Characterization of the ANTARES Photomultiplier R 7081-20

N. Nijenhuis

Characterization of the ANTARES Photomultiplier R 7081-20

Nadjezjda Nijenhuis

Universiteit van Amsterdam
Faculteit der Natuurwetenschappen, Wiskunde en Informatica

Doctoraal scriptie
Supervisors:
Dr. E. de Wolf,
Dr. J. Steijger,
Ing. E. Kok.

NIKHEF
Kruislaan 409
1098 SJ Amsterdam
The Netherlands.

August 2002

Preface

During my internship at the ANTARES group at NIKHEF, I have made a study of the photomultiplier (PMT) that will be used in the detector. In chapter 4, I have made an estimate of the amount of light produced by a muon crossing the detector, that will be incident on a PMT in the detector. This is the amount of light with which the PMT should be tested. The setup to test the PMT I have built together with Erwin Kok, who is also in the ANTARES group at NIKHEF and who came up with the idea of using a VCSEL as light source after the blue LED turned out to be useless. Jos Steijger from the HERMES group at NIKHEF helped with good suggestions on how to improve the setup. In chapter 6, I have analysed the data acquired from the measurements. In order to understand the cause of the so-called out-of-time pulses that arrive on average 3 ns after the in-time pulses, which are the pulses you expect from a PMT, I have had discussions with Hervé Lafoux from DAPNIA, and John MacMillan from the University of Sheffield. The former provided me with a picture of the dynode system in the PMT (see figure 3.7 in chapter 3), the latter offered to lend a nanoled, which unfortunately was too late available.

Abstract

In the Mediterranean sea, 40 km from the coast of Toulon, at a depth of 2400 km a detector, consisting of an array of photomultipliers (PMTs), will be built by the ANTARES collaboration for the detection of high-energy cosmic neutrinos. The detector will detect the Čerenkov light produced by relativistic muons which are created when the cosmic neutrinos interact with the rock below or the seawater surrounding the detector. With the detector it will be possible to measure the energy and the direction of the muons, and thus find the angular position of the source of their parent neutrinos. To be able to do this, the properties of the PMTs used have to be well known and understood. Furthermore a good timing precision is needed ($\sim$ 1 ns) in order to get a good angular resolution (0.2^o for a muon energy above 10 TeV).

In this Master's thesis we have made a study of the charge and time characteristics of the output pulse of the PMT, which will be used in the detector, as a function of the impact point of a light beam on the surface of the PMT. The amount of light used was the same as the amount with which the PMT will have to deal in the detector. We have found that there are, apart from afterpulses, not one but two types of output pulses, whose intensity changes as a function of the position of the impact point. We have tried to explain the cause of the "out-of-time" pulses that arrive 3 ns later than the "in-time" pulses, which are the pulses you expect from a PMT. The regions in which the intensity of the out-of-time pulses is higher than the intensity of the in-time pulses are problem areas since a timing precision of $\sim$ 1 ns is needed to have a good angular resolution. A map of these regions has been made.

Contents

Chapter 1

Introduction

The universe has always fascinated man. First recorded observations were made by ancient civilizations like the Babylonians and the Greeks, who watched the sky with the naked eye through which the sun, the moon, five of the nine planets (Mercurius, Venus, Mars, Saturnus and Jupiter), and the sphere of fixed stars, were visible. The Greek mathematician Aristarchus, who lived from ca. 310-230 B.C.E., was the first to bring forward the idea of the Earth moving around the Sun [1]. Unfortunately this hypothesis was later disregarded by Aristotle and it took until the sixteenth century, when the Polish astronomer and mathematician Nicholas Copernicus argued the same idea in his work *De revolutionibus orbium coelestium* (1543), to be brought forward again [1].

One century later in 1610, Galilei Galileo became the first man to probe the sky by means of a telescope, an instrument that was invented only two years earlier by Hans Lippershey, a spectacle maker from Middelburg [2]. With the help of the telescope he had made himself and which collected about hundred times as much light as the unaided eye, Galileo found that the Milky Way consisted of faint stars, that the moon had mountains, and most importantly, he saw that Jupiter had four small bodies circling around it. He concluded that these bodies move around the far greater mass of Jupiter just as Venus and Mercury, and perhaps the other planets circle around the Sun [2].

Another early observer of the skies through a telescope is Christiaan Huygens. In 1655 he discovered Saturn's brightest satellite Titan with a home-made 12-foot telescope, and explained the arms of Saturn, as being a flat ring, rotating around and unattached to the planet [3]. Together with his brother Constantijn he started building better telescopes. An example of one of them is shown in figure 1.1. This 123-foot aerial telescope has its objective placed on a high tower, without a long tube connecting the objective to the eye piece.

Through the centuries the development of larger and better telescopes continued, making it possible to probe even further into the universe. Nowadays the largest optical telescope is the European Southern Observatory's very large telescope (VLT), located in Chile and consisting of four 8.2 m telescopes, which combined have the same light collecting power as a 16 meter single telescope [4]. With this telescope the most distant group of galaxies ever seen, at a distance of 13.5 billion light-years away, has been discovered on April 9 th 2002 [5]. It takes 0.9 times the age of the universe for

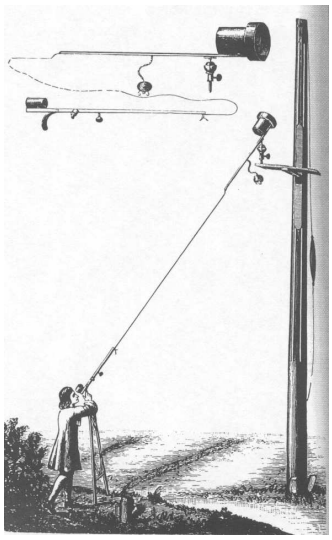

Figure 1.1: *Christiaan Huygens' 123-foot aerial telescope. Picture taken from [3]*

light to cover this distance. We see the group of galaxies as they were when the universe was only 10 % of its present age.

The observable universe, however, is not limited to the optical part of the electromagnetic spectrum. Nowadays astronomy covers the whole spectrum: from radio waves to gamma rays. The latter have an energy of 1 MeV or more, and include the most energetic photons in nature. They have, in contrast to those gamma rays emitted by radioactive sources on and in the Earth, a cosmic origin. This was first pointed out by Victor Hess [1], who had come to this conclusion from electrometer measurements done during a series of high-altitude balloon flights in the period from 1911 till 1912. It took, however, until the 1930s before the cosmic origin of these gamma rays was generally accepted.

Unfortunately gamma ray astronomy is limited to distances of less than 100 Mpc for gamma rays with energies above 10 TeV. This so-called Greisen-Zatsepin-Kuzmin (GZK) cut-off is due to the interaction of the gamma rays with the infrared radiation background, mostly consisting of the cosmic microwave background [6]. This interaction leads to the creation of electron-positron pairs. Since high energy gamma rays from distances further away than 100 Mpc, are not detectable, it seems impossible to say something about their source of origin.

Fortunately, there is a particle, that might be produced in the same processes responsible for the high energy gamma rays, and that can be detected: the neutrino. Its existence was first suggested by Pauli in 1930, and its experimental discovery took place in the mid-fifties of the 20-th century when Cowan and Reines conducted their experiments on a large tank of water at the Savannah River nuclear reactor in South Carolina [7]. The usefulness for probing the universe with neutrinos lies in the fact that they interact only weakly with matter: they are insensitive to the GZK cut-off. Furthermore a neutrino is electrically neutral and thus its path will not be bent by

galactic magnetic fields: it will point directly at its source.

Since a neutrino only interacts with matter via the weak interaction, a large amount of material is needed in order to detect it: a lake or an ocean. The water surrounding the detector will function as a detecting medium, and as a shield for cosmic radiation and sunlight. The idea of a big underwater detector was first put forward by M.A. Markov in 1960 [8], but it wasn't until 1993 before the first underwater neutrino telescope, able to detect high energy cosmic neutrinos, was built in lake Baikal, Russia [9]. The detector, called NT-36, consisted of 36 optical modules (OMs) (see paragraph 2.3 for the definition of an OM) distributed over three short strings, and was situated 1.1 km below the surface of the lake. Currently the detector (NT-200) consists of 192 OMs distributed over eight strings. Another neutrino telescope presently taking data is the AMANDA II telescope, which is situated in the ice of the South Pole [10], and has 677 OMs distributed over 19 strings at depths from 1.3 to 2.4 km. By the end of 2004 the ANTARES project will join them in their search for the origin of high energy cosmic neutrinos [11].

This thesis is about the main component of the ANTARES detector: the photomultiplier (PMT). The time and charge characteristics of its output signal have been measured as a function of the impact point of the light beam on its surface.

Chapter 2 gives a brief overview of the ANTARES project, including the construction of the detector, the detecting principle on which it is based, the time and position calibration of the detector, and the basic principles of track reconstruction. The next chapter gives a description of the construction and characteristics of a PMT. Furthermore the ANTARES PMT is described. In chapter 4 we make an estimate of the amount of light produced by a muon crossing the detector, that will be incident on a PMT in the detector. This is the amount of light with which the PMT has been tested. The setup used for testing the characteristics of the PMT is described in chapter 5. The results obtained with this setup are given in chapter 6, at the end of which an attempt is made to explain these rather strange results. Finally, a general conclusion is given in chapter 7.

Chapter 2

ANTARES

2.1 Introduction

The ANTARES collaboration will build a 0.1 km^2 detector for the detection of high energy neutrinos. The detector will be located 40 km from Toulon (42^o $50'$ N, 6^o $10'$ E), France at a depth of 2.4 km in the Mediterranean sea. It will have a 3.5 π sr coverage of the sky, and will be able to survey the galactic center [12]. With the detector it will be possible to measure the energy and the direction of the detected neutrino. Since a neutrino is neutral, it will point at its source and thus the angular position of the source will be found.

Possible sources of high-energy cosmic neutrinos are those that accelerate protons up to very high energies (above 10^{20} eV). Pions that are formed when these highly energetic protons interact with matter will in their decay produce neutrinos. Examples of sources in our galaxy are supernova remnants and X-ray binaries; examples outside our galaxy are active galactic nuclei (AGN) and gamma ray bursts (GRB). In supernova remnants the accelerated protons interact with the matter of the shell, in X-ray binaries they interact with the accreting matter or the companion star, in GRB with the radiation field of the source, and in AGN with the matter of the accretion disk or its ambient radiation field [12].

This chapter is about how the cosmic neutrinos will be detected, and how their paths will be reconstructed. First the detection principle is described in section 2.2. Then a short description of the detector is given in section 2.3. Calibration of the detector is described in the following section, and finally, the basic principles of track reconstruction are explained in section 2.5, which concludes this chapter.

All of the information given in sections 2.2, 2.3, and 2.4 can be found in more detail in the ANTARES proposal [12] and the technical design report[13]. For details about track reconstruction we refer to the article written by E. Carmona and J.J. Hernández [14].

2.2 Detecting principle

The telescope will be built upon the detecting principle first proposed by M.A. Markov [8] in 1960: the detection of Čerenkov light, produced when relativistic charged particles cross the detector, by an array of PMTs (see chapter 4 for more about Čerenkov light). In our case the charged particles are muons that are formed when muon neutrinos ν_μ or anti-muon neutrinos $\overline{\nu}_\mu$ interact with the Earth or the sea water surrounding the detector (the detector does not make a distinction between neutrinos and anti-neutrinos):

$$\nu_\mu + N \rightarrow \mu^- + X \tag{2.1}$$

$$\overline{\nu}_\mu + N \rightarrow \mu^+ + X \tag{2.2}$$

with N the target nucleon, μ^- a muon with negative charge, μ^+ a muon with positive charge, and X the hadronic final state.

The detector looks downward and so uses the Earth not only as a target but also as a shield for atmospheric muons, which are produced when cosmic rays interact with the atmosphere. Atmospheric neutrinos that are formed in the same process do reach the detector, and are identical to the cosmic ones, except that they are less energetic. By applying a cut to the muon energy they can be eliminated.

With the array of PMTs the number of Čerenkov photons and their arrival times will be measured. From these the energy and direction of the muon can be derived. The direction of the muon neutrino will be almost the same as that of the muon: the angle between them is about 0.7^o for a 1 TeV neutrino.

2.3 The detector

Figure 2.1 shows a schematic view of the detector, which consists of ten 448 m long strings, placed in an octagonal formation with a closest distance between two strings of 60 m. The strings, made of strong electro-optical cables, are anchored to the bottom of the sea, and point upwards due to buoyancy.

A string is built up of 30 storeys, 12 m apart. The first storey is placed about 100 m above the sea bottom. Each storey consists of three optical modules (OMs). An OM is a pressure resistant glass sphere, housing a $10''$ Hamamatsu R 7081-20 photomultiplier (PMT), a high voltage converter to operate the PMT and an electronic circuit, which stores the signals into a buffer. The OMs are positioned in such a way that the three PMTs are oriented away from each other at an angle of 45^o down from horizontal. The PMTs are shielded from the Earth magnetic field by mu-metal cages. A local control module (LCM) and equipment for calibration and positioning are also located at each storey. A string control module (SCM) is placed at the bottom of each string. The SCMs are connected to a common junction box by means of electro-optical cables. The junction box is linked to the shore via a standard deep sea telecommunication cable.

Six analogue ring sampler (ARS) chips (two for each OM), located in the LCM, continuously sample the output pulses of the PMTs, with a tunable frequency between

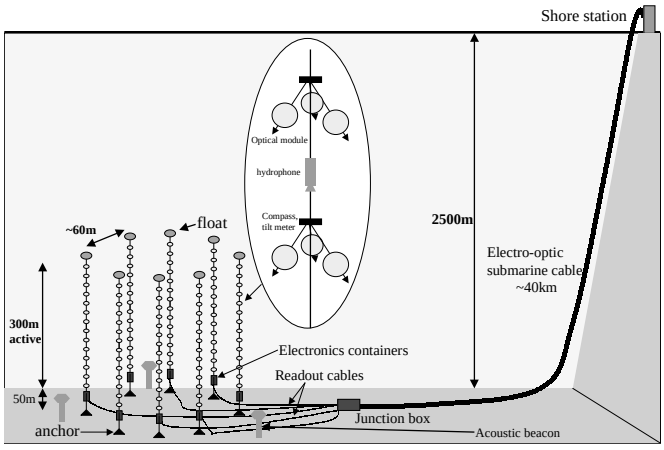

Figure 2.1: *The detector. Picture taken from [12]*

300 and 1000 MHz. An ARS is an application specific integrated circuit, developed for the digital front end. It has an internal clock register, which is stamped when the PMT signal is accepted (the threshold is typically 0.3 p.e.). The clock, located in the LCM, is set by an on-shore Master Clock. Digitization of the signals, stored in the ARS, takes place when a trigger is received. The digital data is sent to the SCM, which collects all the digitized data from the string. From here the data is sent, via the common junction box, to shore where it will be processed.

2.4 Detector calibration

To reconstruct the muon tracks through the detector it is necessary to have a well calibrated detector, both in position and in time.

For the calibration of the relative positions of the OMs, tiltmeters and acoustic positioning are used. The position of an OM has to be monitored continuously, since it changes due to bending of the string by the sea current. A High Frequency Long Baseline acoustic system (HFLBL) gives the 3D position of hydrophones, which are distributed along the strings. With the tiltmeter-compass sensors it is possible to measure the tilt angles of each OM with respect to the horizontal plane as well as its orientation with respect to the Earth Magnetic North. With the information obtained from these measurements it is possible to reconstruct the shape of the strings, and to pinpoint the relative position of an OM up to a precision better than 10 cm, even for a sea current as strong as 15 cm/s. The sea current intensity measured varies from 0 to 19 cm/s, and is on average 6.8 cm/s [15].

LEDs, which are distributed along the strings and in the OMs, function as optical beacons for the time calibration. With the LEDs in the OMs the transit time of the

PMT is calibrated, by firing the LED and measuring the detection time of the photons given by the ARS time stamp. The internal clock in the LCM on its turn is calibrated by measuring the transit time of the clock signal between the on-shore Master Clock and the LCM clock board. The relative time offset of the detector is calibrated by measuring the relative detection times of photons coming from a single source. There are four optical beacons along each string and one laser beacon at the foot of each string that can be used. It should be possible to have a time calibration better than 0.5 ns.

2.5 Track reconstruction

The times of arrival of the Čerenkov photons on the PMTs (the hit times) depend on the position of the PMTs, and on the track parameters position (p_x, p_y, p_z) and direction (θ, ϕ). Thus it is possible to make an estimate of the track parameters of the muon at a fixed time t_0 using the hit times. This is done by first calculating the hit times with the following expression:

$$t_i = t_0 + \frac{1}{c}\left(l_i + r_i \tan\theta_c\right) \tag{2.3}$$

with t_i the time of arrival of the Čerenkov light on PMT i, t_0 the reference time, l_i the distance between the position $\vec{p}$ of the muon at time t_0 and the perpendicular projection of the position of PMT i on the muon's track direction, and r_i the distance between PMT i and its perpendicular projection on the muon's track (see figure 2.2).

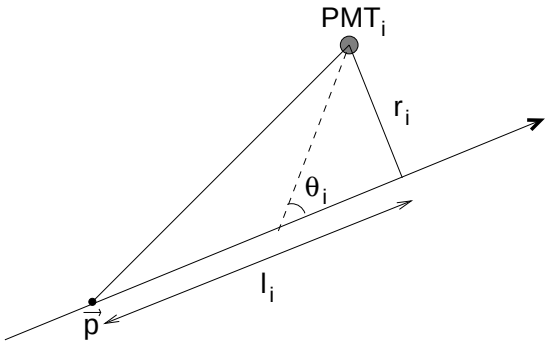

Figure 2.2: *Geometrical relation between a muon track and PMT i.* $\vec{p}$ *is the position of the muon at a reference time* t_0, l_i *is the distance between this position and the perpendicular projection of the position of PMT i on the track direction of the muon,* r_i *is the distance between PMT i and its perpendicular projection on the muon track, and* θ_c *is the Čerenkov angle.*

The difference between the calculated and measured arrival times of the Čerenkov light on the PMTs should be minimized. This is done by estimating for an initial set of track parameters the hit times t_i by using equation 2.3. An estimate is given for the

probability of a given hit to come from the track, based upon the difference between the measured and calculated values. This is done by using a parametrization of the probability density function (pdf) of the arrival times of the photons. The difference has to be minimized to find the muon track.

The process of minimization needs a pre-fit to initialize and guide it. The starting parameters given by the pre-fit should not be far from the real values, in order to avoid failure. For more information on how this is done we refer to the article by E. Carmona and J.J. Hernández [14].

In paragraph 2.2 we have mentioned that the angle between a muon and its parent neutrino is 0.7^o for a 1 TeV neutrino. This means that the uncertainty in the reconstruction of the direction of the muon should be a fraction of this value. When this is the case the inaccuracy in the direction of the neutrino will be dominated by the angle between neutrino and muon. Monte Carlo studies show that with a trigger of at least five PMTs, distributed over at least three strings, a timing precision of $\sim$1 ns is needed to have an angular resolution of about 0.2^o for a muon energy above 10 TeV. Thus the transit time of a photoelectron in a PMT in the detector should have an precision of $\sim$1 ns (see paragraph 3.4.2 in chapter 3 for the definition of transit time).

Chapter 3

The Photomultiplier

3.1 Introduction

In 1887 Hertz discovered, when studying the length of sparks generated by an induction coil, that the length of a spark increased when in its neighbourhood another spark was generated. He found that ultraviolet light emitted by the spark was responsible for this phenomenon. The ultraviolet light caused the emittance of electrons from the negative electrode [16]. The conversion of photons into free electrons is called the photoelectric effect and is described by Einstein in his famous article about quantum theory in 1905 [17]. Five years after Hertz's discovery, Austin and Starke discovered the phenomenon of secondary electron emission when they studied the reflection of cathode rays from metal surfaces. They found that the metal surfaces emitted more electrons than they received [18]. With these two discoveries it was now possible to construct a photomultiplier (PMT).

This chapter is about the construction and characteristics of a PMT. The first section deals with its basic principle. In the next section the mechanical characteristics of the ANTARES PMT R7081-20 are described. Finally the signal properties are discussed in section 3.4, which concludes this chapter.

3.2 Basic principle

A PMT is a vacuum tube consisting of a photo-sensitive cathode (photocathode), focusing electrodes, an electron multiplier and an anode. When light enters the photocathode, photoelectrons are emitted into the vacuum of the tube. These photoelectrons are directed by the focusing electrodes towards the electron multiplier where they are multiplied by the secondary emission electrodes (dynodes). The final total electron flux is collected by the anode.

Figure 3.1 shows an example of the construction of a PMT. Apart from the above mentioned parts, it also shows the input window, which is made of glass. Notice the shape and positioning of the last dynode and anode. The anode is drawn as a dotted line to indicate that it is a grid, through which the electrons emitted at the last but one

dynode pass, to reach the last dynode. There, for the last time, multiplication takes place, and the final electron flux is collected by the anode. Some electrons, however, may be emitted from the anode since all metals show some secondary emission. For this reason the last dynode is bend at the sides to function as an electrostatic screen. The distance between the anode and the last dynode is small so that the electrons coming from the one but last dynode will reach the last one. In order to reduce the accumulation of space charge the magnetic field is strong.

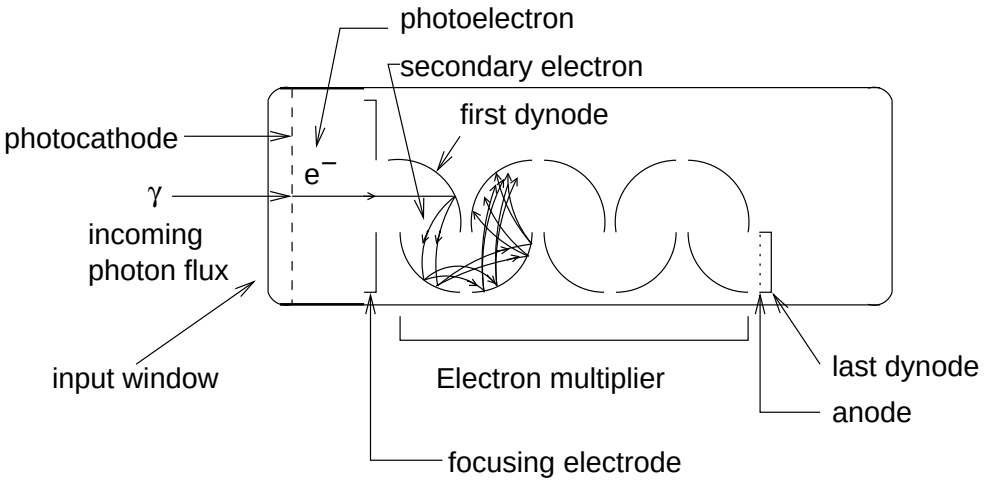

Figure 3.1: *Schematic diagram of a photomultiplier tube. Picture adapted from [19]*

In the remainder of this paragraph the above mentioned parts of the PMT will be described in more detail, concluding with the base, which distributes the input voltage over photocathode and dynodes.

3.2.1 The Photocathode

The photocathode converts incident photons into electrons by the photoelectric effect. It is a semiconductor and can be described by a bandmodel (see figure 3.2). The band structure consists of three regions: the valence band, the energy gap and the conduction band. In the valence band the electrons are bound to the lattice atoms, in the conduction band on the other hand they are free to roam about the entire photocathode. Although called bands, they actually consist of many energy levels, which are so closely spaced that they can be considered a continuum. The energy gap, the region between valence and conduction band, has no energy levels available to electrons to occupy. This is the forbidden region. When the width of the energy gap is small enough, as is the case for a semiconductor, electrons in the valence band can be excited to jump to the conduction band, leaving holes behind in the valence band. If the absorbed energy is high enough they can even cross the vacuum barrier and be emitted into the vacuum of the tube. When an electron in the valence band

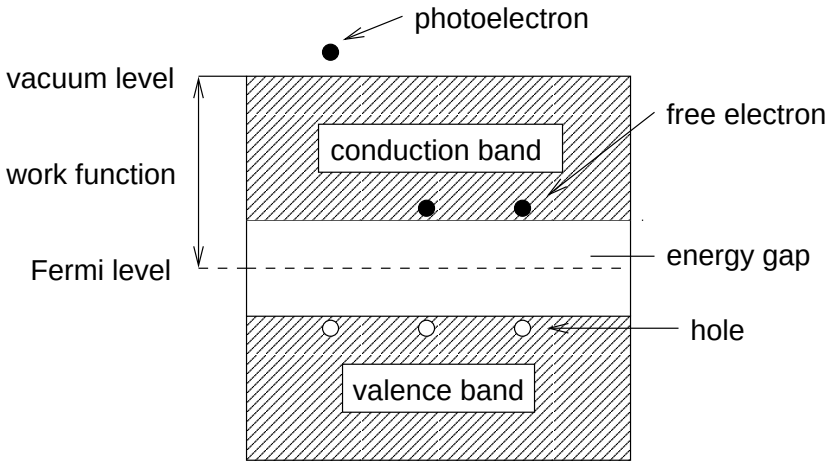

Figure 3.2: *Bandmodel of an alkali photocathode.*

absorbs a photon of energy hν, which is high enough to overcome the vacuum barrier, it is emitted into the vacuum of the tube with an energy given by:

$$E = h\nu - \phi \tag{3.1}$$

with h Planck's constant, ν the frequency of the incident light, and ϕ the work function (the energy difference between the Fermi level and the vacuum level). Only photons with an energy above the threshold value (the work function) may cause the emittance of photoelectrons. The probability for emittance of a photoelectron when the absorbed photon energy is above the threshold value, is not one, but depends on the wavelength of the incident light and on the photoemissive material out of which the photocathode is made. Each incident photon transfers its energy to only one electron. The efficiency of the photocathode in converting photons into electrons, as a function of the wavelength, is expressed by the quantum efficiency $\eta(\lambda)$. It is defined as:

$$\eta(\lambda) = \frac{N_e}{N_\gamma(\lambda)} \tag{3.2}$$

with N_γ the number of incident photons and N_e the number of emitted photoelectrons. The quantum efficiency is a measure for the sensitivity of the photocathode (the spectral response). Figure 3.3 shows a graph of the quantum efficiency as a function of the wavelength for the photoelectric material used in our PMT. The quantum efficiency peaks at a wavelength of 420 nm.

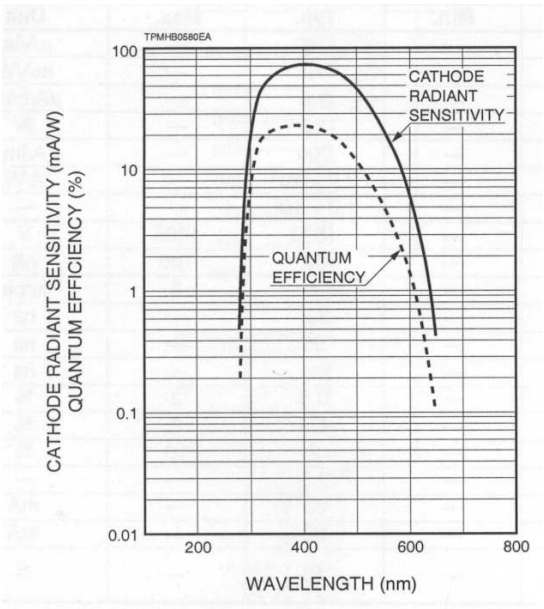

Figure 3.3: *The dotted line shows the quantum efficiency as a function of the wavelength. Also shown is the cathode radiant sensitivity, which is another measure for the spectral response and is defined as the ratio of the photoelectric emission current from the photocathode and the incident radiant power. Picture taken from [20]*

3.2.2 The electron-optical input system

The electron-optical input system is the part between photocathode and first dynode. It directs the emitted photoelectrons towards the first dynode and its design has to meet the following two requirements:

- The collection of the emitted photoelectrons onto the first dynode has to be as efficient as possible and independent of the photoelectrons initial velocity and place of origin on the photocathode. The electric field between photocathode and first dynode should be such that missing the first dynode is very unlikely.
- The time needed for a photoelectron to reach the first dynode must be as independent as possible of its point of departure on the photocathode and its initial velocity.

To meet both of the above requirements focusing electrodes are used (see figure 3.1). The focusing, however, can be affected by external magnetic fields, for example the Earth magnetic field. These can cause the electron paths to deviate from the optimum ones and reduce the efficiency of the PMT. Since the path lengths are longest in the electron-optical input system, the influence of magnetic fields is mostly present in this part of the PMT. The force F_b on an electron due to a magnetic field is proportional to the cross product of the electron velocity and the magnetic field. The force due to the electric field F_e is proportial to the electric field. Since $F_e \gg F_b$, the direction of

the velocity will be almost parallel to the electric field. Keeping the axis of the PMT parallel to the magnetic field will then reduce its influence. Putting a high voltage difference between photocathode and first dynode also reduces the influence of the magnetic field since the higher the energy of the photoelectrons the less sensitive they are to the magnetic field: to bend the path a force proportional to v^2/R is needed, with R the radius of curvature. The best way to decrease the influence of a magnetic field, however, is to put a mu-metal cage around the PMT. Mu-metal has a high permeability and will shield the PMT against external magnetic fields.

3.2.3 The electron multiplier

In the electron multiplier the amplification of the initial photocurrent takes place. For this dynodes are used (figure 3.1). The dynodes are made of secondary emissive material, which emits electrons, called secondary electrons, when hit by an electron of enough energy, called the primary electron. The theory underlying this phenomenon is very similar to that of photoelectric emission except that the incident photon is now replaced by an electron, and that the material used is often a metal, which is a conductor and does not have a threshold. The number of emitted secondary electrons per primary electron is called the secondary emission factor δ of the dynode and depends on the energy of the incident electron. Figure 3.4 shows this dependence for three different secondary emissive materials.

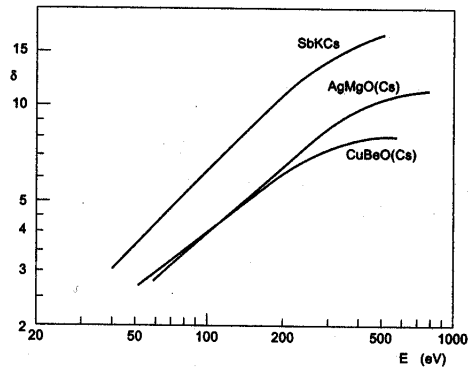

Figure 3.4: *The secondary emission factor δ as a function of the energy of the primary electron, for three dynode materials. The top curve shows the dependence for SbKCs [22].*

The dynode material must meet the following three requirements:

- a high δ;
- the secondary emission is stable under high currents;
- low thermionic emission (noise).

The dynodes are positioned in such a way that the electric field between them causes most of the emitted secondary electrons to reach the following dynode with enough energy to ensure further emittance of secondaries. This will continue throughout the dynode stages and finally a measurable pulse will reach the anode. The charge of the output pulse is the product of the number of electrons in the pulse and the electron charge. The total multiplication (gain) is given by the product of all the δ's times the collection efficiency for each dynode:

$$G = \prod_{k=1}^{N} \alpha_k \delta_k \tag{3.3}$$

with G the gain of the PMT, δ_k the secondary emission factor of dynode k, and α_k the collection efficiency of the interdynode space that follows dynode k. α_k=1 means that all the electrons coming from dynode k reach dynode k+1.

3.2.4 The base

In the base of the PMT the voltage divider is located. The high voltage between photocathode (K) and anode (P) is distributed over the focusing electrodes and dynodes by resistors. The voltage dividing circuit, which we have used, is shown in figure 3.5.

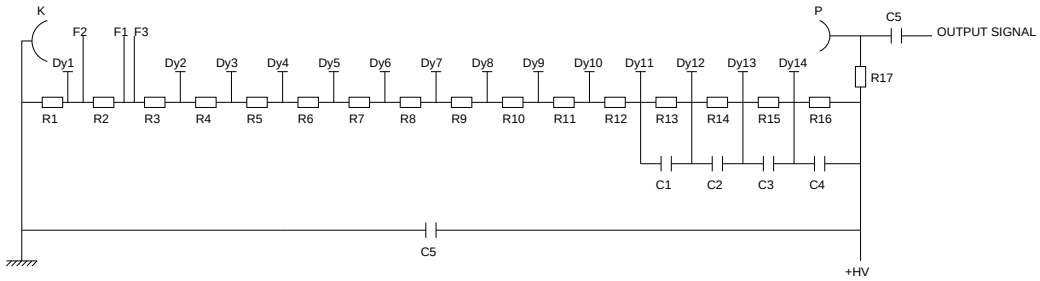

Figure 3.5: *Diagram of the used voltage divider[21].*

The current in the resistance chain, called bleeder current, must be large with respect to the current in the tube. This will prevent the occurence of large potential variations between the dynodes due to changing currents in the tube and will keep the gain as constant as possible. Since the current pulses can be at times very high, especially at the last stages of the multiplication chain, capacitors are used to maintain a fixed potential between the last dynodes. They provide the charge necessary to prevent a potential drop due to a high current pulse. The photocathode is kept at ground potential. This means that the anode is at a positive potential. To filter out the dc component in the output signal, a capacitor is placed after the anode.

3.3 The ANTARES PMT

The ANTARES PMT (R7081-20) is a 10″ hemispherical tube, with a radius of 136.69 mm, made by Hamamatsu. It has a sensitive area of 550 cm^2. Figure 3.6 shows the dimensional outline and a view of the bottom. We will now briefly go through its

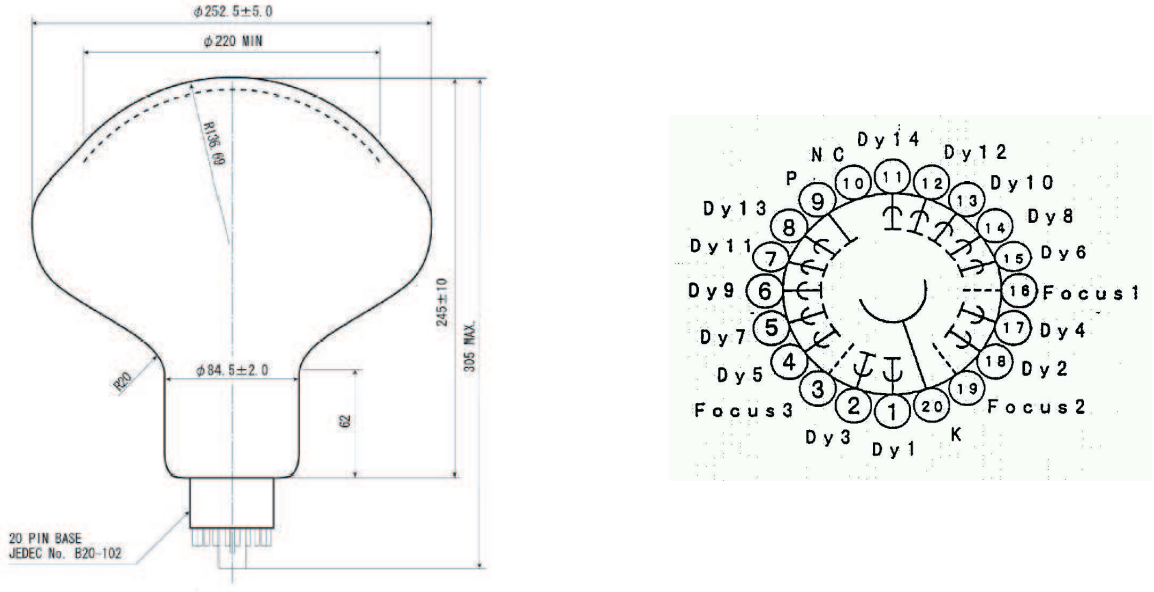

Figure 3.6: *Front and bottom view of the R7081-20 photomultiplier tube. Pictures taken from [23]*

components:

- The input window is made of borosilicate glass. A 3 mm thick layer only transmits light with a wavelength longer than 250 nm. Its transmission is optimal (near 100 %) for wavelengths of about 350 nm and longer [22].

- The photocathode has a diameter of 220 mm (minimal) and is almost spherical. It is made of bialkali (SbKCs) and most sensitive in the blue to violet region of the spectrum (see figure 3.3).

- The 14 stage dynode configuration is box and line (figure 3.7). This is a combination of a so-called box and linear focusing configuration. The box structure has a large collection area at the first dynode, but a low electric field at the internal surface of the boxes, giving rise to a larger transit time, and a wider transit time spread. Transit time and transit time spread are explained in the following paragraph. In the ANTARES experiment a low transit time spread is important. The linear focusing type, on the other hand, has a good focusing throughout all the dynode stages, which reduces the variation in transit time. Thus taking the first dynode to be of the box type, and the rest of the dynodes of the linear focusing type, we get a dynode configuration, which has a large collection area at the first

dynode and a good focusing at the latter stages. Like the photocathode, the dynodes are made of bialkali (SbKCs), which has the required high δ (see figure 3.4);

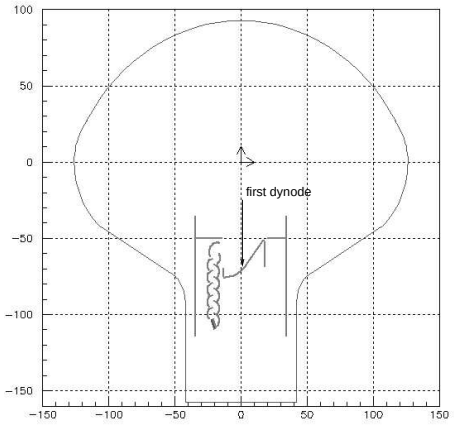

Figure 3.7: *View of the position of the electron multiplier in the PMT [24].*

- The base used is the 20-pin base JEDEC B20-102 (10 cm in diameter) [23]. The voltage dividing circuit was already shown in figure 3.5. The resistor values have been measured and are shown in table 3.1. Also shown are the results of measurements performed by Hamamatsu on a slightly different base. The difference between the two bases lies in the resistor used between the photocathode and the first dynode. Hamamatsu used a 1.1 MΩ resistor, we used a 2.2 MΩ resistor.

3.4 Characteristics

The main characteristics of a PMT fall into two classes. The first class deals with the charge of the PMT output pulse, the second with its timing. In the following a description of these characteristics will be given. Furthermore the development of the pulse shape, dark current and afterpulses will be described.

3.4.1 Charge spectrum

The distribution of the charge of PMT output signals shows the fluctuations in the multiplication of electrons in the electron multiplier. Since we are testing the PMT at one photoelectron level, for reasons explained in the following chapter, we will be dealing with a so-called single photoelectron spectrum (SPE spectrum), see figure 3.8. This spectrum is in good approximation Gaussian: the number of emitted electrons at each dynode stage is Poisson distributed. The total number of emitted electrons is also Poisson distributed, but can be approximated by a Gaussian distribution since the average number of electrons is large. Characteristics like the gain (G), the peak to

Resistor	MΩ (Hamamatsu)	MΩ	dynode	V(V)
R1	1.13	2.20	K	0
R2+3	0.40	0.39	Dy1	857.70
R4	0.50	0.47	Dy2	1009.75
R5	0.3333	0.34	Dy3	1192.99
R6	0.167	0.18	Dy4	1325.54
R7	0.1	0.10	Dy5	1395.72
R8	0.1	0.10	Dy6	1434.71
R9	0.1	0.10	Dy7	1473.70
R10	0.1	0.10	Dy8	1512.69
R11	0.1	0.10	Dy9	1551.68
R12	0.12	0.12	Dy10	1590.67
R13	0.15	0.15	Dy11	1637.45
R14	0.22	0.22	Dy12	1695.93
R15	0.30	0.33	Dy13	1781.70
R16	0.24	0.23	Dy14	1910.35

Table 3.1: *Base composition. The second column shows the result for the Hamamatsu base [25]. The third shows ours. The calculated potential at each dynode for a total supply voltage of 2000 V is shown in the last column.*

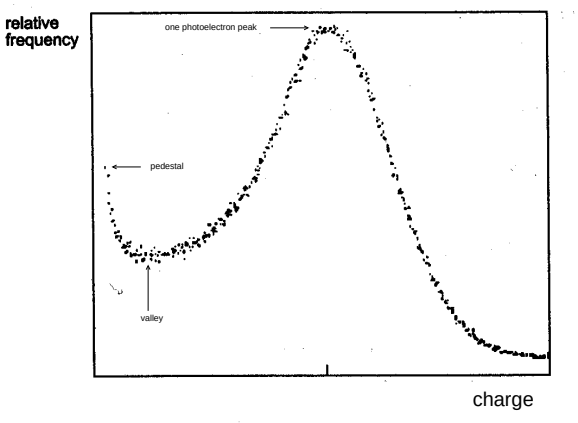

Figure 3.8: *Typical SPE spectrum [22].*

valley (P/V) ratio and the energy resolution can be obtained from the SPE spectrum.

G is a measure of the electron multiplication and is defined as the ratio between the current through the anode (I_a) and the photoelectric current (I_k):

$$G = \frac{I_a}{I_k} \tag{3.4}$$

It can be obtained from the SPE spectrum, through the position of the SPE peak, which gives the mean charge of the output signals. Dividing this by the charge of one electron gives the gain. The gain can also be calculated using equation 2.3. The δ value for each dynode can be found by calculating the voltage difference between two consecutive dynodes. The voltage difference between any two dynodes can be calculated from the resistor values in the base, shown in table 3.1. These potential differences can be used to estimate δ. In table 3.2 this calculation is done for a supply voltage of 2000 V.

	ΔV	Dynode	δ
K-Dy1	857.70	K	1
Dy1-Dy2	152.05	Dy1	17.2
Dy2-Dy3	183.24	Dy2	8.8
Dy3-Dy4	132.55	Dy3	10.1
Dy4-Dy5	70.18	Dy4	7.9
Dy5-Dy6	38.99	Dy5	4.7
Dy6-Dy7	38.99	Dy6	2.9
Dy7-Dy8	38.99	Dy7	2.9
Dy8-Dy9	38.99	Dy8	2.9
Dy9-Dy10	38.99	Dy9	2.9
Dy10-Dy11	46.78	Dy10	2.9
Dy11-Dy12	58.48	Dy11	3.4
Dy12-Dy13	85.77	Dy12	4.0
Dy13-Dy14	128.65	Dy13	5.5
Dy14-P	89.67	Dy14	7.68
		Total gain	6.7×10^9

Table 3.2: *Dynode gains and total gain at a supply voltage of 2000 V. Also shown are the voltage differences between two consecutive dynodes.*

The (P/V) ratio is the height of the SPE peak divided by the height of the valley. It gives an indication of the resolution: the larger its value, the better the SPE events can be distinguished.

The energy resolution is defined as the ratio of the FWHM of the SPE peak to its position. FWHM stands for full width at half maximum and is the width of the peak at half its height.

The energy resolution is equivalent to ΔG/G, with ΔG/G given by:

$$\left(\frac{\Delta G}{G}\right)^2 = \sum_{i=1}^{14}\left(\prod_{j=1}^{i}\frac{1}{\alpha_j\delta_j}\right) \tag{3.5}$$

with δ_j the gain of dynode j and α_j the collection efficiency of the space between dynode j and dynode j+1. The dominant contribution to the energy resolution comes from the first dynode. The higher the gain of the first dynode the better the resolution will be. The gain of the first dynode is 17.2 (see table 3.2). Thus ΔG/G = 25 %, and the FWHM of the SPE spectrum is about 60 %. The last step is possible because the

SPE spectrum is in good approximation Gaussian and for a Gaussian distribution the following relation between the standard deviation σ and the FWHM of the distribution is valid: FWHM = 2.35σ.

3.4.2 Time characteristics

The two time characteristics are the transit time (TT) and the transit time spread (TTS).

The TT is the time between illumination of the photocathode by a short light pulse, and the arrival of the current pulse on the anode. It is inversely proportional to the square root of the supply voltage. The emitted photoelectron is non-relativistic: its kinetic energy (E_k) is much smaller than its rest mass (m_e) ($E_k < 2$ keV, $m_e \approx 500$ keV). Using the classical equations of motion will give the inverse proportionality.

The TTS is the FWHM of the transit time distribution. It is proportional to $1/\sqrt{n_e}$, with n_e the number of emitted photoelectrons, and depends on the size and shape of the photocathode, on the voltage applied to the tube and on the wavelength of the incident light. The time distribution is in good approximation Gaussian. It shows the distribution of the time it takes for the arrival of an output pulse on the anode and does not depend on the duration of the output pulse. In the extreme case of one photoelectron per event, the variation in the arrival time of an output pulse on the anode will be maximum. The variation will decrease with the number of photoelectrons emitted at the same time from the photocathode. The photoelectron arriving first on the first dynode will in general cause the start of the output on the anode. The arrival time of the start of the output pulse depends on the time the first photoelectron reaches the first dynode. Thus the more photoelectrons there are per event, the less the variation in arrival time of the first photoelectron on the first dynode will become. Since the distribution is Gaussian, the FWHM is proportional to $1/\sqrt{n_e}$. The size and shape determine the photoelectron path lengths between photocathode and first dynode. Different lengths will cause a spread in transit time. The voltage applied over the tube will determine the time it takes to cross the paths. The higher the voltage, the shorter the time per path and the smaller the time differences. The energy of the emitted photoelectron and thus its departure speed from the photocathode depends on the wavelength of the incident light. The higher the energy the shorter it takes for a photoelectron to cross a path, and the smaller the TTS will be.

Difference in departure speeds from the photocathode, and difference in path lengths between photocathode and first dynode, are the main causes of variation in transit time. Ideally the time distribution should be measured with delta function light pulses. Since this is, in our case, not possible the lightsource should have a FWHM much less than that of the time distribution.

3.4.3 Pulse shape

The rise and fall time of the anode output pulse are, assuming the lightsource to be a delta function, defined as follows: the rise time is the time it takes for the anode pulse to increase from 10 to 90 percent of its amplitude. The fall time is the time

it takes the pulse to decrease from 90 to 10 percent, and is in general two or three times larger than the rise time [19]. The smearing of the delta function shape, when only one photoelectron is emitted from the cathode surface, is due to the electric field distribution between the dynodes, causing a spread in arrival times of the electrons on the anode.

3.4.4 Dark current

When a PMT is operated in an absolutely dark environment, it should not have any output signal. This, however, is not the case. The output current is called the dark current and is mainly caused by:

- Thermionic emission current from photocathode and dynodes. These, due to their low workfunction, emit thermionic electrons. At room temperature it is the dominating cause of the dark current. Its contribution decreases, however, when the PMT is cooled;
- Leakage current. This contributor to the dark current is caused by leakage in the insulation. It increases linearly with the supply voltage, via Ohm's law:

$$I_l = \frac{V}{R_i} \tag{3.6}$$

  with I_l the leakage current, V the supply voltage and R_i the insulation resistance;
- Field emission. Some electrons will be emitted by the electric field, when the PMT is operated at a very high voltage. This will shorten the PMT's lifetime. In the specification sheet, supplied by Hamamatsu, it is given that the supply voltage between anode and photocathode should not be more than 2000 V [23];
- Photocurrent, produced by scintillation of the glass envelop or electrode supports, due to stray electrons;
- Background radiation. This has two main causes. One is the production of Čerenkov light by cosmic rays, mostly muons, that pass through the glass envelope. The other is the emission of beta rays by the isotope ^{40}K, since the envelop glass contains potassium oxide (K_2O).

3.4.5 Afterpulses

Afterpulses are pulses that can follow the main pulse. There are two kinds of afterpulses:

- Those that are caused by photons, emitted by the last dynodes in the chain due to the electron bombardment. They find their way back to the photocathode, where they are converted into photoelectrons. Their delay is several nanoseconds to several tens of nanoseconds;
- Those caused by the ionisation of residual gasses in the PMT, whose positive ions return to the photocathode. Their delay is much longer, due to the ion mass. It can be hundreds of nanoseconds to several microseconds.

Apart from afterpulses, there are also prepulses and late pulses. Prepulses are caused by photons that have no interaction in the photocathode and reach the first dynode where they cause the emission of photoelectrons. Late pulses are produced when the photoelectron is intercepted and reflected by the potential grids before it reaches the first dynode.

In table 3.3 a list of the possible time intervals between the after-, pre- and late pulses and the main pulse is given. These values are taken from the specification sheet for the R7081-20 [23].

Type of pulse	Time before/after the main pulse (ns)
pre	10-100 (before)
late	25-100 (after)
after	100-16000 (after)

Table 3.3: *Possible time intervals between after-, pre- and late pulses and the main pulse. Values are taken from [23].*

Chapter 4

Photoelectrons

4.1 Introduction

The ANTARES detector looks at muons, which are produced when muon-neutrinos interact with the rock or sea-water surrounding the detector. These muons emit Čerenkov light when passing through the sea water, which is detected by photomultipliers. Čerenkov light is emitted when the velocity of the particle is higher than the speed of light in the traversed medium: $\beta > 1/n$, with $\beta = v/c$ and n is the refractive index of the medium. The light is emitted in a cone. The angle between the direction of propagation of the muon and of the emitted light is given by (see figure 4.1):

$$\cos\theta = 1/n\beta \tag{4.1}$$

For a more detailed description of the theory, which was developed by Tamm and Frank, see [27].

The Čerenkov angle depends on the refractive index of the sea water and the velocity of the muons. We can take the muons to be ultra-relativistic: $\beta = 1$. The refractive index depends on the wavelength and is 1.35 for a wavelength of 450 nm [12]. Inserting these values in equation 4.1 gives a Čerenkov angle of 42^o.

In the following section this value for the Čerenkov angle will be used to make a rough estimate of the average number of photoelectrons that are emitted when the PMT is hit by photons coming from one muon, crossing the detector. This estimate gives us an indication of the amount of light we have to use when testing the PMT. The light source will be such that roughly the same number of photoelectrons will be emitted in the PMT in our set-up as in a PMT in the detector. To verify that this is the case we have to measure the number of emitted photoelectrons. This can be done by using the fact that the number of photoelectrons are Poisson distributed. How this is done is discussed in section 4.3.

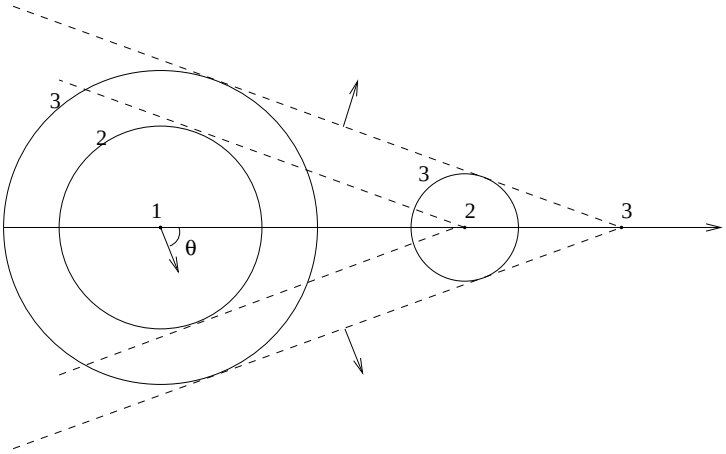

Figure 4.1: *Čerenkov angle. The muon is moving from left to right. At three instances of time its position is indicated by the numbers 1, 2 and 3 along its path (straight line). The light emitted at these positions is drawn at the subsequent times (circles). The propagating wavefront (dotted lines), which is the tangent to the circles drawn at the same instance of time, makes an angle with the path of the muon: the Čerenkov angle. Figure taken from [28]*

4.2 Number of photoelectrons

A simplified picture is used for estimating the number of photons arriving on a PMT. Only Čerenkov photons are considered, leaving out of the calculation photons originating from bremsstrahlung. Also not taken into account are processes like diffusion and multiple scattering. Absorption is considered to be the process responsible for removing Čerenkov photons from the detector.

For a particle with unit charge the number of emitted Čerenkov photons per unit wavelength, per unit path length is [27]:

$$\frac{\mathrm{d}^2 N}{\mathrm{d}x\,\mathrm{d}\lambda} = 2\pi\alpha \frac{\sin^2\theta(\lambda)}{\lambda^2} \tag{4.2}$$

with α the fine structure constant. For wavelengths shorter than 300 nm the light is absorbed by the optical module surrounding the PMT [29]. For wavelengths longer than 600 nm the quantum efficiency of the PMT is low (see figure 3.3 in chapter 3). Integrating over the absorption length from 300 to 600 nm and taking the refractive index and thus the Čerenkov angle constant ($\theta = 42^o$), which is a good approximation, we get for the total number of emitted photons per unit path length:

$$\frac{\mathrm{d}N}{\mathrm{d}x} = 342\ \text{photons/cm} \tag{4.3}$$

In the ANTARES detector the strings, on which the PMT's are grouped, are 60 m apart. An average distance of 30 m from a track to a PMT is a good approximation.

Taking into account absorption we now multiply the yield (equation 4.2) with the transmission. The transmission is given by:

$$T = e^{-\frac{l}{\lambda_a}} \tag{4.4}$$

with λ_a the absorption length and $\ell = 30$ m (the distance between the track and the PMT) (see table 4.1). The result is shown in figure 4.2. Integrating over the wavelength

Wavelength (nm)	Absorption length (m)	Transmission (ℓ = 30m)
307	6.6667	0.0111
330	9.2593	0.0392
350	14.925	0.1340
370	20.000	0.2231
390	26.316	0.3198
410	34.483	0.4190
430	43.478	0.5016
450	50.000	0.5488
470	62.500	0.6188
490	58.824	0.6005
510	50.000	0.5488
530	29.412	0.3606
550	17.857	0.1864
570	16.129	0.1557
590	8.8496	0.0337
610	4.5045	0.0013

Table 4.1: *Absorption length and transmission in sea water for several wavelengths of light [30].*

from 300 to 600 nm gives an average of 95 photons in a ring with a radius of 30 m and a height of 1 cm (the variation of the radius with the height can be neglected). Dividing this by the surface area of the ring (18850 cm^2) gives the number (5 10^{-3}) of photons per cm^2. After multiplication with the surface area of a PMT, facing into the direction of the light (452 cm^2), an average of two photons is found. For values at different PMT distances from the track, see table 4.2.

To get an estimate of the number of photoelectrons, we have to multiply the yield with the transmission of the sea water and the quantum efficiency of the PMT cathode surface. For values of the latter as a function of the wavelength see figure 3.3 in chapter 3. The result is shown in figure 4.3. Integrating over the wavelength and taking into account the size of the area in which the photons are distributed and the size of a PMT in the same way as was done above, an average of 0.4 photoelectrons is found. For values at different distances between track and PMT, see table 4.2.

Distance (m)	Number of incident photons	Number of photoelectrons
5	37.47	6.34
10	14.51	2.51
15	7.76	1.36
30	2.27	0.40
35	1.67	0.30
40	1.26	0.22
45	0.98	0.17

Table 4.2: *Average number of photons incident on a PMT and average number of converted photons for several track-PMT distances.*

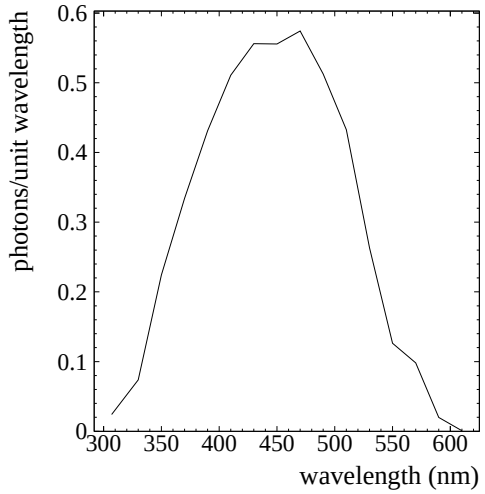

Figure 4.2: *Average number of photons per unit wavelength, in a ring with a radius of 30 m, as a function of the wavelength.*

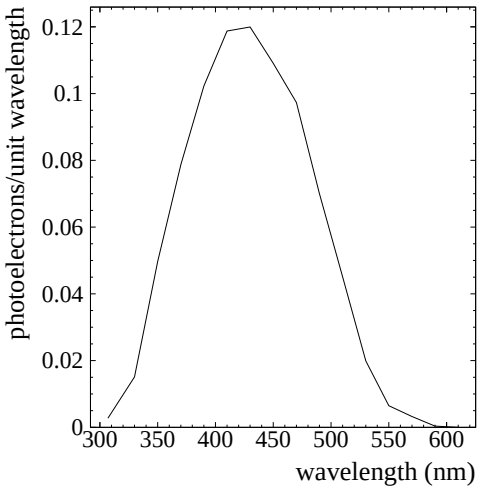

Figure 4.3: *Average number of photoelectrons per unit wavelength, in a ring with a radius of 30 m, as a function of the wavelength.*

4.3 Measuring the number of photoelectrons

In the previous paragraph we have made an estimate of the average number of photoelectrons, which are emitted by the cathode of a PMT in the detector. The characteristics of the PMT have to be measured under similar circumstances as in the detector. Thus when testing the PMT in our setup we have to use a light source, which causes the emission of about one photoelectron per light flash. The high voltage (HV) over the PMT should be such that all events are measured. Its value is chosen by recording a *plateau curve*. The events are counted as a function of the HV. A typical curve is shown in figure 4.4. It shows a flat plateau at which all the events are measured. The supply voltage should be set within this region. The ending of the plateau is caused by noise.

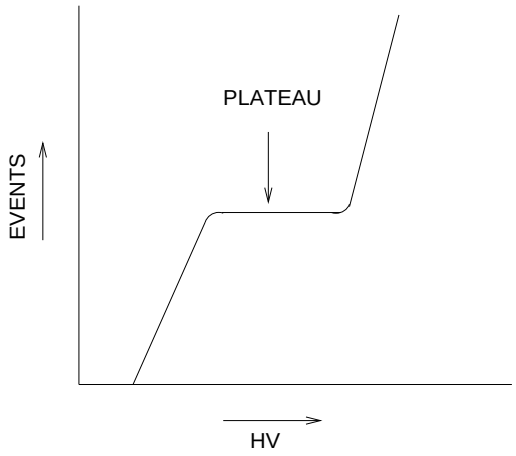

Figure 4.4: *A typical plateau curve. The flat region indicates the plateau at which all events are measured. The rise at the ending of the plateau is due to noise.*

To make sure that when testing the PMT we are working at one photoelectron level we have to measure the average number of photoelectrons, which are emitted per incident light flash. This can be done by using the fact that the number of photoelectrons are Poisson distributed. The Poisson distribution is given by the following relation:

$$P(r;\langle n\rangle) = \frac{e^{\langle -n\rangle}\langle n\rangle^r}{r!} \tag{4.5}$$

With P the probability of obtaining r events if the mean expected number is $\langle$n$\rangle$. This equation simplifies if we only look at the probability of obtaining zero events:

$$P(0) = e^{-\langle n\rangle} \tag{4.6}$$

Thus if we measure the probability of obtaining zero photoelectrons we can calculate the average number of photoelectrons.

Measuring P(0) is done by measuring the number of times that we have a signal from the light source and a signal from the PMT (N_c) in coincidence, and the number of times there is a signal from the light source (N_s):

$$P(0) = 1 - \frac{N_c}{N_s} \tag{4.7}$$

These measurements are done with the use of scalers (see chapter 5).

In summary of the above we see that we can expect an average of 0.4 photoelectrons coming from the cathode of a PMT in the detector. The light source used for testing the PMT should be such that for light flashes hitting the PMT an average of about 0.4 photoelectrons or less is emitted, in order to have a low probability of detecting more than one photoelectron in the same event. The HV over the PMT is set at a value at

which all events are measured. Using the fact that the number of photoelectrons are Poisson distributed, we can verify that the PMT characteristics are measured at one photoelectron level.

Chapter 5

Experimental Setup

In this chapter the experimental setup is described. The first section discusses the light source, used in this experiment. The second deals with the positioning of the PMT and the laser. In the third the signal processing is described, and finally in section 5.4 the light source and the setup, which were initially used, are briefly discussed.

5.1 The light source

There are two properties of the source that have to be considered: the wavelength and the width of the light pulse.

The wavelength of Čerenkov light incident on a PMT in the ANTARES detector is in the blue region of the spectrum, as can be seen in figure 4.2. The quantum efficiency of our PMT is optimal in this region (figure 3.3 in chapter 3). Thus the best possible wavelength for our light source will be 420 nm.

Secondly, the width of the light pulses is important. For instance, when measuring the transit time spread (TTS) we do not want the measured spread to be caused by the width of the used ligth source. In its final test sheet Hamamatsu gives a value of 3.310 ns for the TTS of our PMT [26]. Any light source used should have a width smaller than this. A width of picoseconds is preferable.

In summary the best possible source has a wavelength of 420 nm and a width of picoseconds. Such a source, however, was not available. Since for a TTS measurement the width of the light pulse is more important than the wavelength, we have chosen to work with a vertical cavity surface emitting laser (VCSEL). Its wavelength of 850 nm is far from optimal but its width is small enough for a TTS measurement. This can be seen in figure 5.1 in which the width of the time distribution of the PMT signals, measured with a TDC, is plotted against the width of the current pulse for the VCSEL, measured with a scope. For a width of the current pulse wider than 20 ns, the width of the time distribution of the PMT signals changes linearly with that of the current pulse. In this region the measured spread in the PMT signals is caused by the width of the current pulse. For widths smaller than 20 ns we see that the width of the time distribution is independent of that of the current pulse. In this region we can measure the TTS of the PMT.

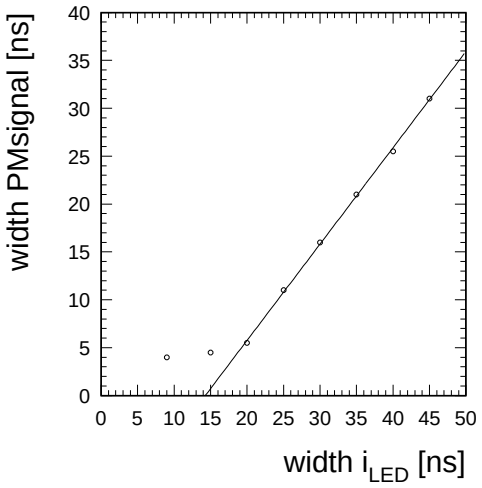

Figure 5.1: *The FWHM of the time distribution of the PMT signals plotted against the width of the current pulse for the VCSEL .*

5.2 Positioning of PMT and VCSEL

The PMT is placed in a holder (see figure 5.2). Its lowest point is 17.7 mm above the ground and it faces in the south-west direction, parallel to the surface it stands on. A measurement of the magnetic field at the position of the PMT shows that it is orientated $8^o \pm 2^o$ from the magnetic South. This is due to machinery, surrounding the PMT and containing iron.

Figure 5.2: *The PMT placed in its holder.*

A plastic disc with a radius of 13.5 cm, on which a coordinate system is defined, is positioned around the front of the PMT at the level of the axis going though the center of the PMT (14.5 cm above the ground) (see figure 5.3). The VCSEL is placed on this disc. There is a small block between laser and PMT with three entrance holes for the laser (-45^o, 0^o and 45^o angles with the normal to the PMT surface) and one exit hole (0^o with the normal to the PMT surface) for the laser light (figure 5.4). There is no need to place any kind of absorber between VCSEL and PMT since, due to the very low quantum efficiency at the wavelength of the VCSEL light (850 nm), we are automatically at one photoelectron level.

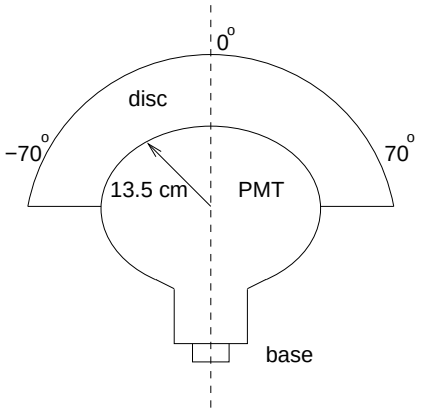

Figure 5.3: *Top view of the disc surrounding the PMT.*

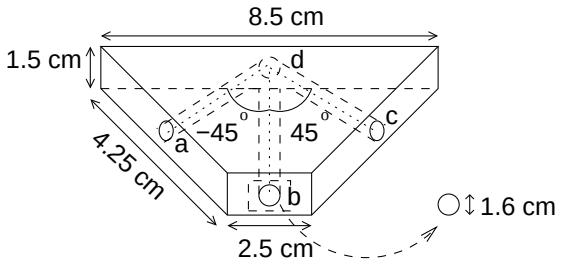

Figure 5.4: *Block used between laser and PMT. There are three entrance holes for the laser (a, b and c) and one exit for the laser light (d).*

The PMT and laser setup is placed in a 115×50×77 cm^3 light-tight aluminium box, which is painted black on the inside. Holes are made on one side to allow cables for PMT and laser to go through. Black tape is used to cover the parts, which were left open, to make sure no light enters. For the same purpose a black cloth covers the entire box.

5.2.1 Reference frames

There are two coordinates used. The first, θ, was already mentioned above and is used to pinpoint the position of the laser to the PMT. The scale on the disc goes from -90^o to 90^o with 0^o situated on the main axis of the PMT. By changing the position of the laser on the disc a measurement of the characteristics of the PMT as a function of θ can be made (see figure 5.5).

The second coordinate ϕ is the angle around the base of the PMT (see figure 5.6). The scale goes from 0^o to 360^o in steps of 15^o, with 0^o at the notch, indicated in figure 5.6. On top of the holder a marker is placed, which can be best viewed in figure 5.2. This enables us to measure the PMT characteristics as a function of ϕ (figure 5.5), by

turning the PMT in its holder and indicating with the marker the angle belonging to the chosen ϕ-orientation of the PMT. Note that with the θ scans the magnetic field is fixed. With the ϕ scans on the other hand, the PMT rotates in the Earth magnetic field, and its orientation with respect to this field changes.

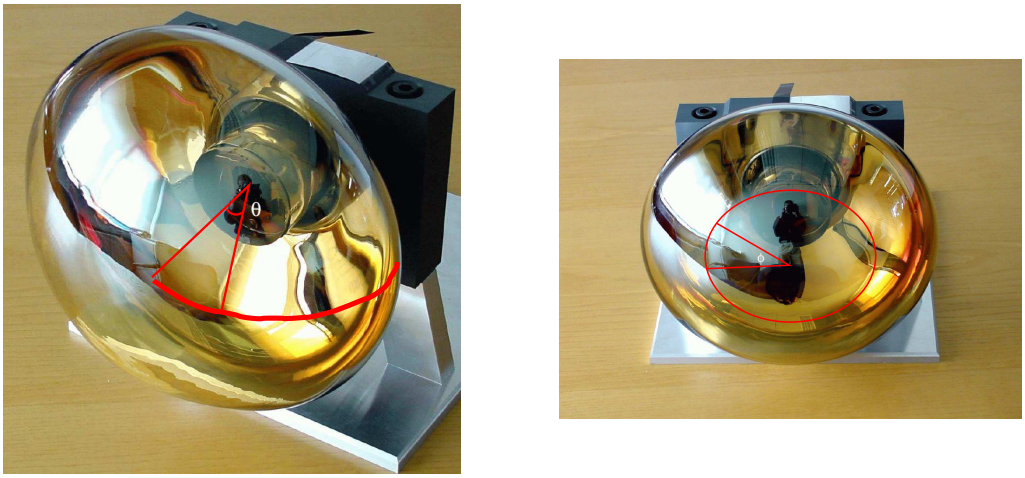

Figure 5.5: *Directions of the θ scan (left picture) and ϕ scan (right picture) of the PMT.*

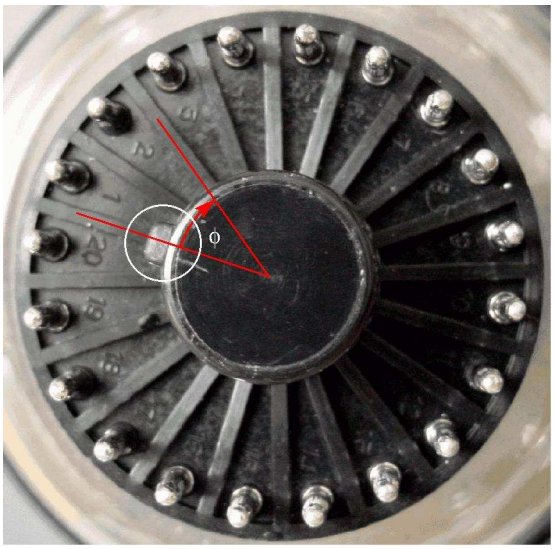

Figure 5.6: *The base of the PMT to which the ϕ-coordinate system is attached. The white circle indicates the point at which ϕ is taken to be zero.*

5.3 Signal processing

Two different kinds of measurements are done. One is a measurement of the charge distribution of the PMT signals, for which an ADC (LeCroy 2249SG) is used. The other is a measurement of the timing characteristics, for which we use a TDC (LeCroy 2228A).

A schematic overview of the entire setup is given in figure 5.7. Both PMT and laser are situated in the box. The rest of the setup is located outside the box. The high voltage supply for the PMT is provided by a CAEN 40 channel high voltage system (SY 127).

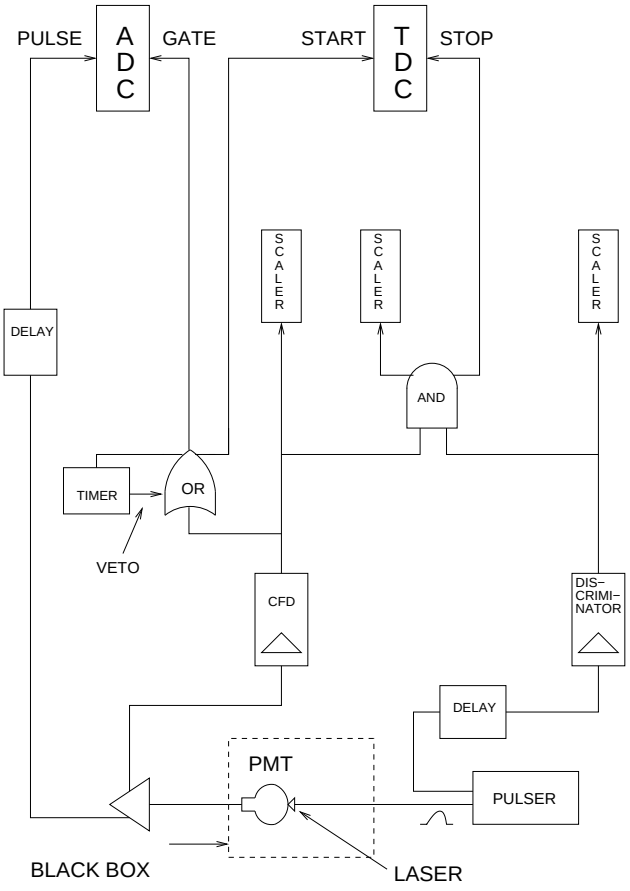

Figure 5.7: *Schematic overview of the setup.*

The laser is driven by a pulse generator (PM 57868) at a frequency of 11.75 ± 0.05 kHz. The pulses from the pulse generator have an amplitude of 2.54 ± 0.01 V , a rise time of 10.6 ± 0.1 ns, a fall time of 0.9 ± 0.1 ns and a FWHM of 6.3 ± 0.1 ns. This is the minimum possible width. At this width, as can be seen in figure 5.1, timing measurements can be done. An amplitude of 2.54 V is chosen to have enough events and still be at one photoelectron level.

Two outputs from the pulse generator are used. One output pulse activates the VCSEL, the other is delayed and shaped. After the delaying and shaping, it is split again, used as input for a scaler (LeCroy 2551), with which the frequency of the current pulses is measured and used as input for an AND-port (LeCroy 622). The other input for the AND-gate comes from the PMT.

The output signal of the PMT goes into a bufferamplifier. One output is delayed and measured by an ADC. The other is shaped by a constant fraction discriminator (CFD, Ortec 934). A CFD is used to eliminate *walk*. The shaped signal is split in three. One part of the signal split is used as input for a scaler, with which the frequency of the PMT signals is measured. Another goes into an OR-gate and is stretched to 2 ms, and used as a veto. Of the two outputs of the OR-gate one starts the TDC, the other goes into the gate of the ADC. The veto of 2 ms is there to make sure that only one PMT-pulse at a time is measured by the ADC. The third part, as mentioned above, is used as input for an AND-gate. The output of the AND-gate stops the TDC and is used as input for a scaler, which counts the number of coincidences (see paragraph 4.3).

In summary of the above. We use three scalers. One to count the PMT signals, one to count the current pulses and one to count the number of times we have a signal from the PMT and a current pulse, and thus a flash from the laser, in coincidence.

We have chosen to start the TDC with the PMT signal, to increase the efficiency and stop it with a coincidence, to separate events from background. The background events show up as overflows.

All the modules are placed in a CAMAC crate, and are read out by a computer.

5.4 Blue LED

Some of the early measurements have been done with a blue LED. The LED was driven by a Sheffield pulser [31]. The Sheffield pulser is a two transisor circuit derived from that of Kapustinsky [32], and fabricated commercially for the Sheffield University.

During the measurements the LED was positioned outside the black box. Its light was attenuated to the 1 pe level with the help of absorbers and transported into the black box by means of an optical cable. The end of the fibre was placed about 30 cm in front of the center of the PMT. The PMT was completely illuminated. A pick-up coil around the LED lead was used as a trigger for the stop of the TDC.

This source was later disregarded due to the too large width of its pulses, but some of the results obtained with it are shown in the following chapter.

Chapter 6

Results

6.1 Introduction

In this chapter the results of the measurements are shown, which were obtained when the PMT was tested at the one photoelectron level (1 pe level). The first section includes a plateau curve, a darkcount measurement, some measurements obtained with the blue LED, and some obtained with the VCSEL. The following sections show the results of the θ and ϕ scan (see chapter 5 for their definition). They include the dependence of the transit time (TT), the transit time spread (TTS), the average number of photoelectrons, the gain, the peak to valley ratio, and the energy resolution on the position of the VCSEL on the surface of the PMT . In section 6.5 the influence of the external magnetic fields on the TT, the average number of photoelectrons, and the gain is given. Measured late pulses are shown in section 6.6. Finally, in section 6.7, in which a summary of the results is given, we try to explain why the time distribution has a double peak structure.

6.2 First investigations

In this section some of the early results are shown. They include the darkcount rate as a function of time, a gain vs high voltage, and a TT vs high voltage curve. These last two curves were obtained with the blue LED. Furthermore, an example of a time distribution obtained with this light source is given. Apart from these results all other results shown were obtained with the VCSEL. They include a plateau curve, and time distributions obtained when the PMT was fully and partially illuminated by the VCSEL.

The time distribution, obtained with the blue LED illustrates the necessity of a light source with a width smaller than the TTS of the PMT. The time distributions obtained when the PMT was completely and partly illuminated show the need for a thorough scanning of the surface of the PMT.

6.2.1 Darkcount rate

For measuring the dark current, the black box, containing the PMT, was opened and then closed again. Immediately after closing, we started measuring the darkcount rate at a supply voltage of 2100 V: every ten seconds the number of PMT output pulses, crossing the threshold of the discriminator, was counted. The result is shown in figure 6.1. Based upon this result, we have chosen to wait five to six hours, after opening the

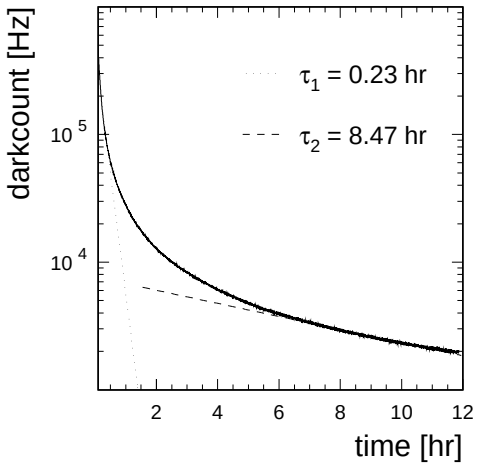

Figure 6.1: *Measured darkcount rate at a high voltage of 2100 V. The beginning, and end of the curve are fitted with exponentials whose characteristic times are* τ_1*, and* τ_2 *respectively.*

black box, before starting a new measurement. The darkcount rate will then be about 4 kHz. This is low compared to the rate after one hour, which is about 30 kHz. As can be seen from the figure, the darkcount rate keeps decreasing after six hours but to wait longer than six hours between two measurements was not possible since this would mean that only one measurement per day could be done. Keeping the time the black box is open as short as possible, will keep the darkcount rate as low as possible.

6.2.2 Blue LED

Arrival time vs HV

Since the time measured is the TT plus the time spent in the electronics, we will call this time the arrival time. Its dependence on the supply voltage is shown in figure 6.2. The zero is taken arbitrarily. Since only the TT depends on the HV, it in fact shows the variation of the TT with the HV. The points are fitted with t_a = -53.4+3778.9/$\sqrt{\text{HV}}$. It is a good fit and thus the data is in agreement with the statement in paragraph 3.4.2 saying that the TT is inversely proportional to the square root of the supply voltage.

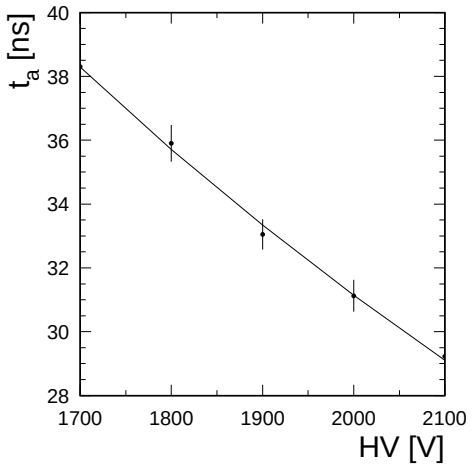

Figure 6.2: *Measured dependence of the arrival time (t_a) on the HV.*

Gain vs HV

The gain is obtained from the position of the SPE peak by multiplying the ADC channel number of the peak with 0.25 pC and dividing it by 1.6×10^{-19} C (the charge of one photoelectron). Figure 6.4 shows the dependence of the gain on the supply voltage. The curve is fitted with an exponential: $G = 2.5\times10^{4}\exp(0.4HV)$.

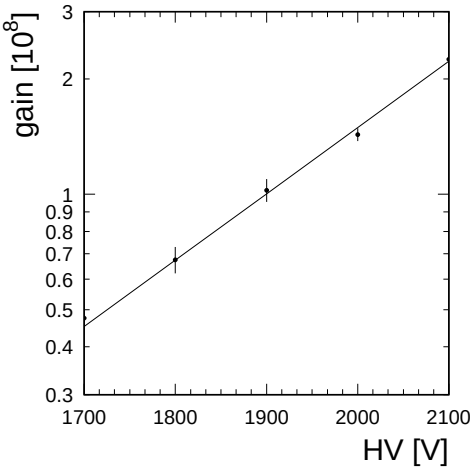

Figure 6.3: *Measured dependence of the gain on the HV.*

TTS

Figure 6.4 shows the FWHM of the time distribution obtained at a supply voltage of 2100 V.

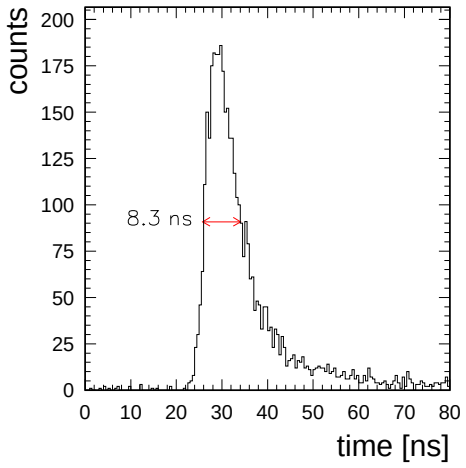

Figure 6.4: *Measured time distribution, obtained with a blue LED placed 30 cm in front of the center of the PMT, at a high voltage of 2100 V.*

Both the PMT and the light source contribute to the FWHM:

$$\text{FWHM} = \sqrt{\text{FWHM}_{led}^2 + \text{TTS}^2} \tag{6.1}$$

with FWHM_{led} the width of the light source. Hamamatsu gives in its test sheets a value of 3.310 ns for the TTS, although obtained with a slightly different base (see paragraph 3.3 in chapter 3), and at a supply voltage of 1850 V [26]. The measured value of 8.3 ns is much too high to be due to the PMT, and so it must greatly be due to the LED. We can conclude that we are looking at the LED and not at the PMT.

With the VCSEL this is not the case as can been seen from figure 5.1 in chapter 5. Thus from now on the results shown, are those obtained with the VCSEL.

6.2.3 Plateau measurement

Figure 6.5 shows the measured plateau curve. The PMT was completely illuminated by the VCSEL, which was positioned at a distance of 30 cm from the PMT, in the black box. From the figure we see that the curve keeps rising. This rising can be caused by randoms. We can calculate the number of randoms: the gate of the AND-gate, with which the coincidences were measured, is open for about 30 ns. The pulser has a flash rate of 11.8 kHz. The darkcount rate at 2100 V is 2 kHz (see figure 6.1). The number of randoms per second at 2100 V will then be 1 Hz (40 ns times 11.8 kHz times 2 kHz

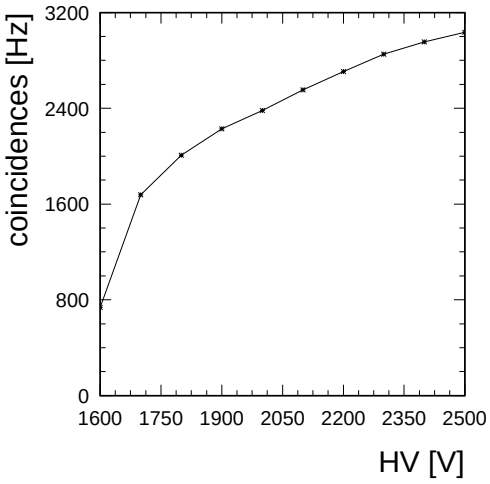

Figure 6.5: *Measured plateau curve, at a discriminator level of 30 mV.*

per second). Thus randoms can not be the cause of the rise. We must conclude that we are not yet on the plateau. Since the maximum supply voltage, given by Hamamatsu [23], is 2000 V, the measurements can not be done on the plateau and a correction has to be made on the average number of photoelectrons measured.

6.2.4 Time distribution

Figure 6.6 shows the time distribution obtained when the PMT was fully illuminated by the VCSEL, which was placed about 30 cm in front of the center of the PMT. The zero is taken arbitrarily, but will be the same for all the time distribution plots obtained with the VCSEL.

Two peaks are seen, about 2.4 ns apart. A possible explanation for the occurence of two peaks, instead of one, is that the first peak is caused by photoelectrons coming from the central region of the PMT, and the second, which is later, is caused by photoelectrons coming from the periferal region. These photoelectrons arrive later because the quality of the field in this region is less than in the central region. To test this assumption, we have done two other measurements. In the first the central region was covered by a black plastic disc with a diameter of 11.5 cm. In the second the plastic sheet from which the disc was taken, was put between laser and PMT, covering all of the PMT except the central disc, with a diameter of 11.5 cm (see figure 6.7).

The results are shown in figure 6.8. We see that the distributions differ. The periferal can be fitted with two Gaussians. The assumption that the second distribution in figure 6.6 is entirely due to photoelectrons coming from the periferal region is wrong. There is still a contribution from what we thought were photoelectrons coming from the central region. This contribution, however, is much less than it is in the central distribution. Apparently the time distribution depends on which part of the PMT is

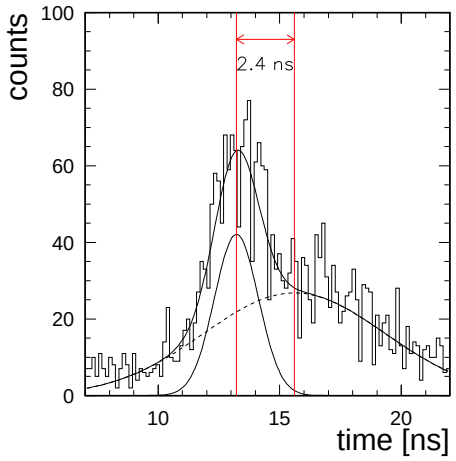

Figure 6.6: *Measured time distribution of the PMT, fully illuminated by the VCSEL, which was positioned 30 cm in front of the center of the PMT. The high voltage was 2300 V.*

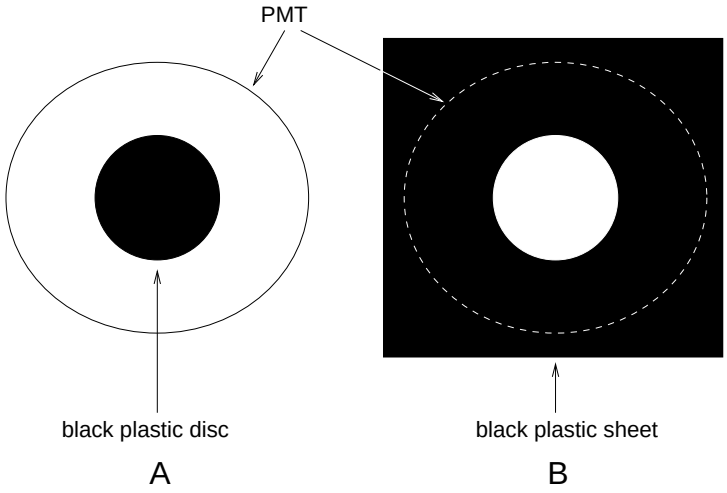

Figure 6.7: *A: the plastic black disc with a diameter of 11.5 cm, covering the central region of the PMT. B: the plastic black sheet, covering all but the central region of the PMT.*

illuminated. To see if and how all of the characteristics of the PMT depend on the position of illumination a scan of the surface has been made. The results are shown in the following paragraphs.

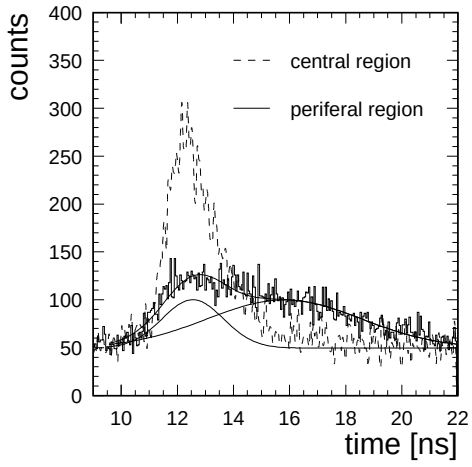

Figure 6.8: *Measured time distributions of respectively the central and periferal region of the PMT. The VCSEL was placed 30 cm in front of the center of the PMT. The high voltage was 2300 V. The periferal region has been fitted with two Gaussians with peak positions at 12.6 and 15.8 ns, and a constant background of 49.6 counts.*

6.3 Time spectrum

The surface of the PMT has been scanned in the ϕ and θ direction. For the θ scan, ϕ was kept fixed at 150^o. For the ϕ scan θ was kept fixed at 50^o.

All of the results shown, except for the TT as a function of the HV curve, were obtained at a high voltage of 2300 V.

6.3.1 Fitting procedure

The double peak structure of the time distribution, which was first seen, when the PMT was completely illuminated by the VCSEL (see figure 6.6), is present at every point of the surface scanned. It can be separated into two distributions, whose intensity changes from point to point. Figure 6.9 shows three examples. The distribution on the left of each plot is called the in-time distribution, because its charge spectrum corresponds to a SPE spectrum (see figure 6.15 in paragraph 6.4.1). The distribution containing events that arrive later is called the out-of-time distribution.

All of the time spectra have been fitted with two Gaussians. The fits cover the spectra from an arrival time t_a = -8 ns to t_a = 42 ns, and are good fits. To estimate the measuring errors, the measurement at ($\theta = 50^o$, $\phi = 150^o$) has been done twice, giving measuring errors on the arrival time (0.4 ns for both in- and out-of-time), and on the TTS (0.07 ns for the in-time, 0.04 ns for the out-of-time). These plus the fitting errors are the errors shown in the plots. The error in the position is 2^o.

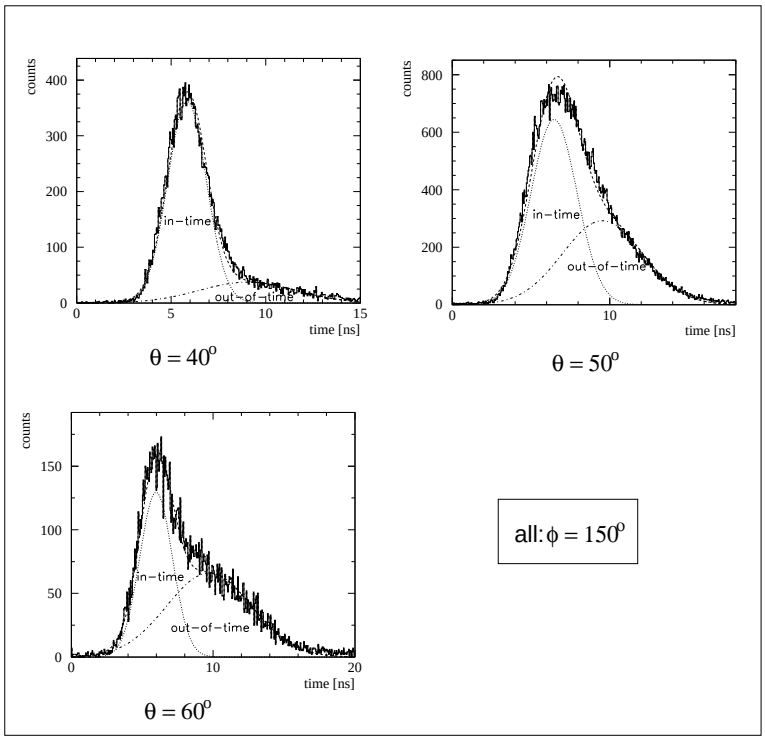

Figure 6.9: *Three examples of the double peak structure of the time distributions, obtained with the VCSEL positioned at ($\theta = 40^o$, $\phi = 150^o$), ($\theta = 50^o$, $\phi = 150^o$), and ($\theta = 60^o$, $\phi = 150^o$) respectively. All spectra were fitted with two Gaussians. The distribution on the left of each plot is called the in-time distribution, the one on the right is called the out-of-time distribution. The high voltage was 2300 V.*

6.3.2 Arrival time vs HV

Figure 6.10 shows the dependence of the arrival time on the supply voltage, for both the in-time and out-of-time distribution at ($\phi = 150^o$, $\theta = 50^o$). Since only the TT depends on the HV, it in fact shows the variation of the TT with the HV. Plotted are the positions of the peaks of the distributions. The in-time points are fitted with t_a = -66.891 + 3411.5/$\sqrt{\text{HV}}$. It is a good fit and thus the data is in agreement with the statement in paragraph 3.4.2 saying that the TT is inversely proportional to the square root of the supply voltage. The out-of-time points are fitted with t_a = -60.795 + 3264.3/$\sqrt{\text{HV}}$. Their delay time is larger than that of the in-time events for each supply voltage. The difference can be fitted with a constant and is 2.9 $\pm$ 0.4 ns.

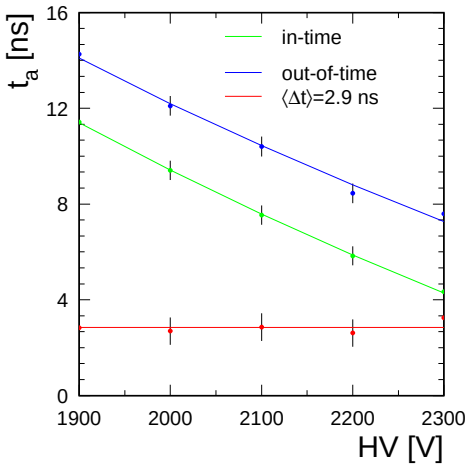

Figure 6.10: *Measured in-time and out-of-time arrival times as a function of the high voltage. The VCSEL was positioned at ($\theta = 0^o$, $\phi = 150^o$).*

6.3.3 Arrival time

The dependence of the arrival time, and thus of the TT on the position is shown in figure 6.11. The left plot shows the dependence on θ with ϕ fixed at 150^o, the right plot the dependence on ϕ with θ fixed at 50^o.

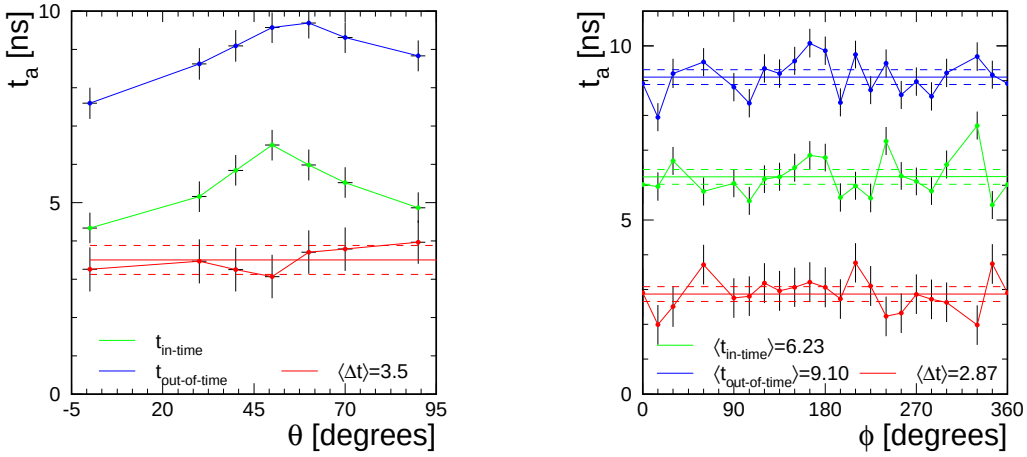

Figure 6.11: *Measured dependence of the in-time and out-of-time arrival times on θ (left plot), and ϕ (right plot). The arrival times were obtained at a high voltage of 2300 V.*

For the θ dependence most of the data was taken in the periferal area of the PMT, since it is in this part of the PMT that the out-of-time distribution is prominently visible. From the figure we see that there is a 2.0 $\pm$ 0.4 ns variation in TT of both the in-time and out-of-time distribution as a function of θ. The difference in arrival time between the two distributions, also shown in figure 6.11, has been fitted with a line of zero slope. Fitting with a slope gave an error on the slope of the same order of magnitude as the slope itself (slope: 0.8×10^{-3}, error:1.2×10^{-2}). Thus the time difference is statistically compatible with a constant and its value is 3.5 $\pm$ 0.4 ns.

The arrival time, and thus the TT is quite independent of ϕ for both the in-time and out-of-time distribution. The out-of-time pulses arrive 2.9 $\pm$ 0.2 ns later than the in-time pulses.

From the above we can conclude that the transit time of both the in-time as out-of-time events varies with θ but is independent of ϕ. Furthermore we see that the out-of-time pulses arrive on average 3.3 $\pm$ 0.4 ns later than the in-time pulses.

6.3.4 TTS

The TTS as a function of the position is shown in figure 6.12. The left plot shows

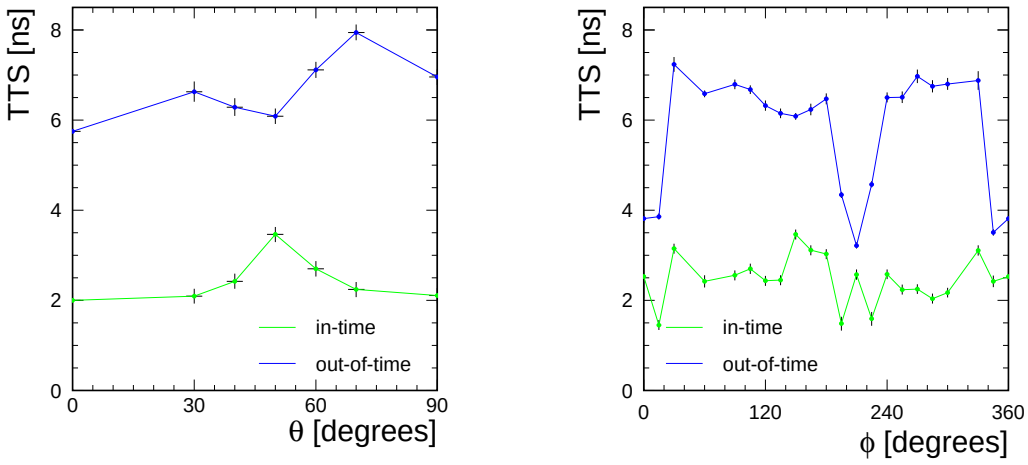

Figure 6.12: *Measured dependence of the in-time and out-of-time TTS on θ (left plot), and ϕ (right plot). The high voltage was 2300 V.*

the dependence on θ. The average value of the FWHM of the in-time distribution is 2.4 $\pm$ 0.4 ns. It is quite stable at about 2 ns, but has a bump at 50^o. The FWHM of the out-of-time distribution, on the other hand, shows a small dip at 50^o, and has on average a value of 6.7 $\pm$ 0.4 ns, which is 4.3 ns larger than that of the in-time distribution.

The right plot of figure 6.12 shows the dependence on ϕ. The FWHM of the in-time distribution varies from 1.5 to 3.5 ns and has on average a value of 2.5 $\pm$ 0.2 ns. The out-of-time TTS is quite independent of ϕ for the regions $30^o \leqq \phi \leqq 180^o$, and

$240^o \leqq \phi \leqq 330^o$, at which it has an average value of 6.6 ± 0.2 ns. It has a dip for $195^o \leqq \phi \leqq 225$, and $345^o \leqq \phi \leqq 15$ at which its average value is 3.9 ± 0.2 ns.

From the above we can conclude that the FWHM of the out-of-time distribution is allways larger than that of the in-time distribution, independent of the position on the surface of the PMT at which the light enters.

6.3.5 Average number of photoelectrons

From the measured number of coincidences, and laser flashes the average number of photoelectrons (pe's) has been calculated (see paragraph 4.3 in chapter 4). Since, as figure 6.5 shows, we are not yet on the plateau at 2300 HV, the measured number of pe's has to be modified. Extrapolation of the curve shows that the number of coincidences will lie around 3200 per second. At 2300 V the measured number per second is 2381. Thus the measured number of pe's has to be multiplied with 1.3 to get the actual average number of pe's.

Since both in-time and out-of-time distributions are fitted with a Gaussian, their relative intensities can be calculated with:

$$I = \frac{A\sigma\sqrt{2\pi}}{N} \tag{6.2}$$

with I the relative intensity, A the amplitude , σ the sigma of the distribution and N the number of events in the distribution. Calculating the relative in-time and out-of-time intensities and multiplying these with the measured average number of pe's gives the average number of pe's of the in-time and out-of-time distribution.

In calculating the error on the average number of pe's the error taken into account is the error on the number of coincidences, which is taken to be the inverse of the square root of the number of coincidences. This error, and the error found by doing the measurement at ($\theta = 50^o$, $\phi = 150^o$) twice gives the error on the average number of pe's:

$$\Delta pe = \sqrt{(\Delta pe_1)^2 + (\Delta pe_2)^2} \tag{6.3}$$

with Δpe the total error, Δpe_1 the error found from the estimated error on the number of coincidences, and Δpe_2 the error found from measuring the number of pe's twice at the same position.

To estimate the error on the average in-time and out-of-time pe's, the errors on the relative intensities are also needed. These were found from redoing the measurement at ($\theta = 50^o$, $\phi = 150^o$), giving a measuring error on the in-time intensity of 0.04, and on the out-of-time intensity of 0.05. The fitting errors can be neglected.

The dependence of the average number of pe's on the position is shown in figure 6.13. The average number of pe's of the in-time distribution decreases from the center to the edge of the photocathode. This drop is not due to a drop in gain. The gain does drop from center to $\theta = 50^o$, but after $\theta = 50^o$ it rises again slightly (see figure 6.17 in paragraph 6.4.3). The in-time pe's, on the otherhand, keep decreasing after $\theta = 50^o$. The average number of pe's of the out-of-time distribution is quite constant. For $\theta > 50^o$ the average number of out-of time pe's is larger than, or within the error

bars, the same as the in-time pe's. Since $\theta = 50^o$ is a turning point, the variation with ϕ has been measured at this θ position.

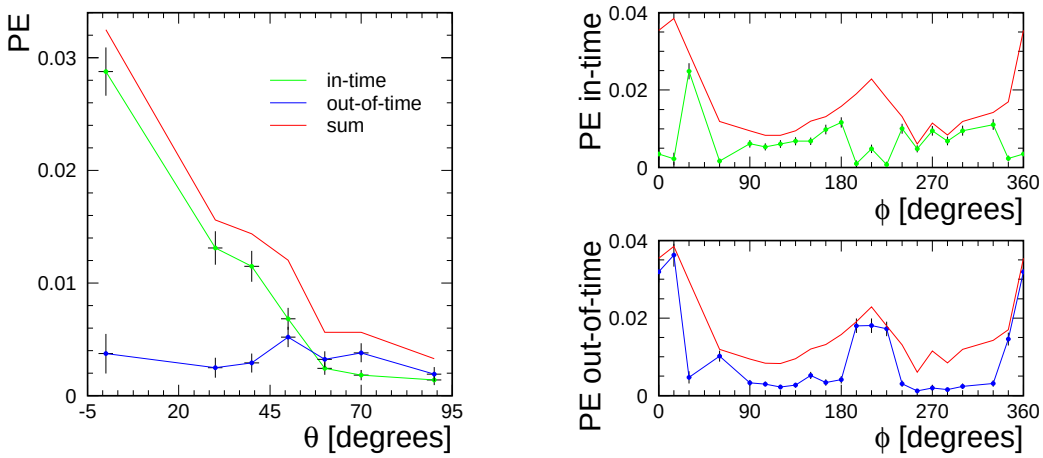

Figure 6.13: *Measured dependence of the average number of in-time and out-of time photoelectrons on θ (left plot), and ϕ (right plot). The high voltage was 2300 V.*

The dependence of the average number of pe's on ϕ differs from that of the gain (see figure 6.17 in paragraph 6.4.3). There are two regions and one angle at which the average number of out-of-time pe's is larger than the average number of in-time pe's. The two regions are $345^o \leqq \phi \leqq 15^o$, $195^o \leqq \phi \leqq 225^o$, and the angle is ϕ=60^o. At ϕ=150^o the pe's of the out-of-time curve show a rise. Probably at this position the number of out-of-time pe's is larger than the number of in-time pe's, but the reason that we do not actually see this, is because the VCSEL was not exactly at the position on the PMT at which this occurs. This assumption is in agreement with the details of the construction of the PMT, shown in figure 6.14. A symmetry axis can be drawn through $\phi = 105^o$ and $\phi = 285^o$. The regions $345^o \leqq \phi \leqq 15^o$ and $195^o \leqq \phi \leqq 225^o$ are each others mirror image. The mirror image of ϕ=60^o is ϕ=150^o.

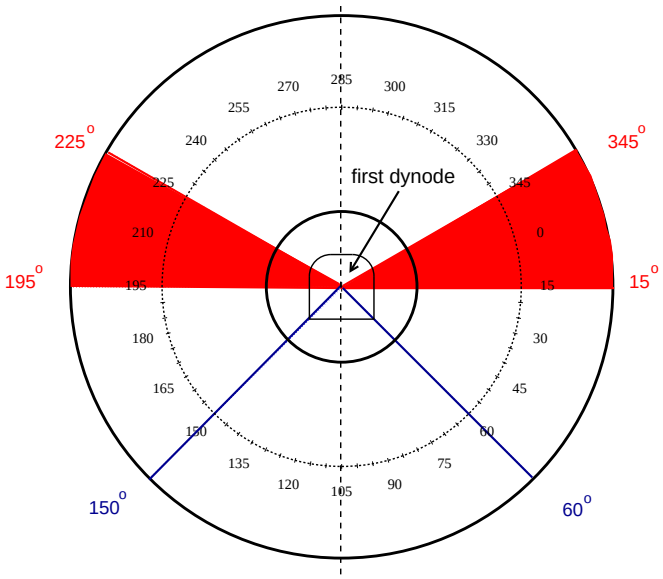

Figure 6.14: *Front view of the PMT. The cross-section at $\theta = 50^o$ is indicated, as well as the orientation of the ϕ positions to the first dynode. The dotted line indicates the symmetry axis of the PMT. The red areas are the areas in which the average number of out-of-time pe's is larger than the average number of in-time pe's. These are also the areas in which the TTS of the out-of-time pe's is low (3.9 ± 0.2 ns) compared to the other areas which have an average value of 6.6 ± 0.2 ns (see paragraph 6.3.4). The blue lines show the orientation of the position at ($\theta = 50^o$, $\phi = 60^o$) at which the average number of out-of-time pe's is also larger than the average number of in-time pe's, and the orientation of its mirror position ($\theta = 50^o$, $\phi = 150^o$). All is on scale.*

6.4 Charge spectrum

6.4.1 Fitting procedure

The time distribution can be separated into two distributions. To see if events in these distributions differ from each other in their charge characteristics, the charge spectrum has to be split into a spectrum containing only in-time events and one containing only out-of-time events. To do this we have taken for the in-time contribution to the charge

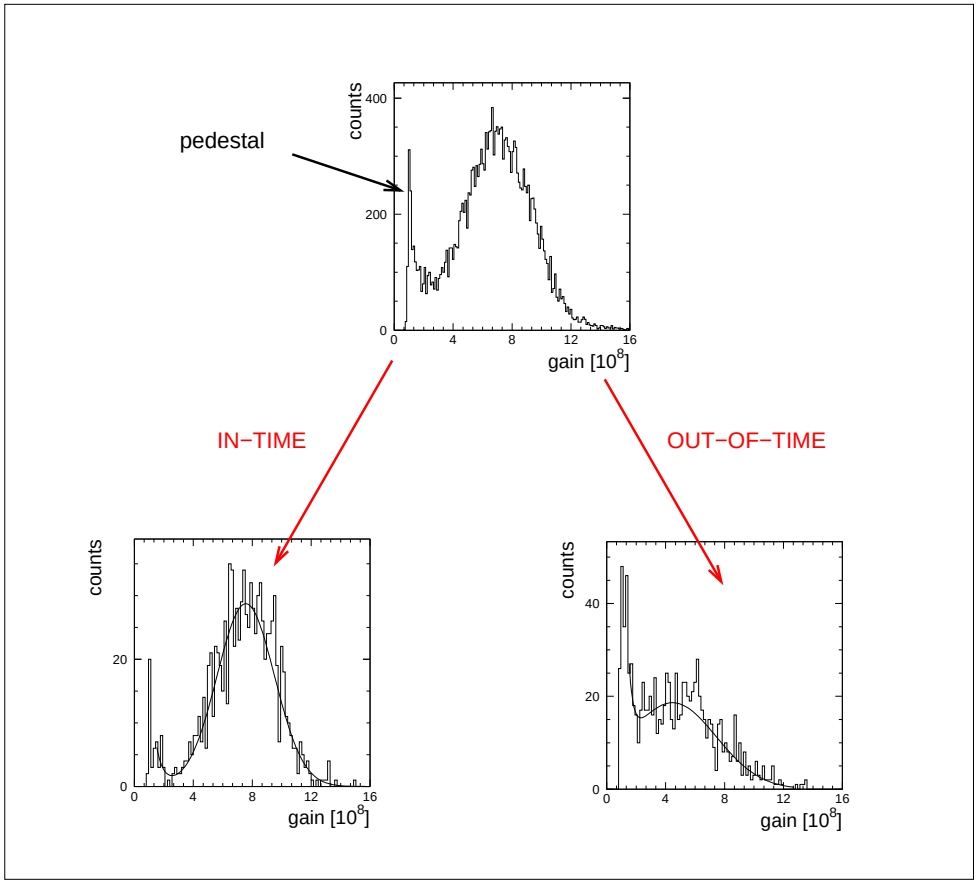

Figure 6.15: *Splitting of the charge spectrum into an in-time (the SPE spectrum), and an out-of-time spectrum. Both spectra were fitted with a Gaussian and an exponential. The VCSEL was positioned at ($\theta = 0^o$, $\phi = 150^o$). The high voltage was 2300 V.*

spectrum, the first 1000 events with an arrival time $t_a = 2$ and higher, and for the out-of-time contribution the last thousand events with $t_a = 14.5$ and lower. Thus we have taken the events in the tails of the time distribution. Only a thousand events are taken to be sure that the in-time charge distribution contains only in-time events and that the out-of-time contains only out-of-time events. This is the case when the intensity of the in-time distribution is much larger than the out-of-time. When the

intensity of the out-of-time time distribution is much larger than that of the in-time, the in-time charge spectrum will contain some out-of-time events, but their number is neglegible compared to the number of in-time events. When the intensity of the out-of-time time distribution is about the same as that of the in-time there will be some out-of time events in the in-time charge distribution, but their number is too small to have an influence.

An example of a splitting of a charge distribution into an in-time and out-of-time part is shown in figure 6.15 for ($\theta = 0^o$, $\phi = 150^o$), and a supply voltage of 2300 V. The figure shows that, apart from the pedestal, the in-time and out-of-time charge distributions differ from each other. The pedestal is the positive shift of the spectrum due to an intrinsic shift of the ADC and to the darkcurrent. Both in-time, and out-of-time distributions are fitted well with a Gaussian and an exponential.

The spectrum has been measured twice at the position ($\theta = 50^o$, $\phi = 150^o$). The difference in gain between both measurements lies within the fitting errors. Thus the errors shown in the plots are only the fitting errors.

6.4.2 Gain vs HV

The measured gain vs HV for both the in-time and out-of-time distribution, with the VCSEL positioned at ($\theta = 0^o$, $\phi = 150^o$), are plotted in figure 6.16. Both curves are

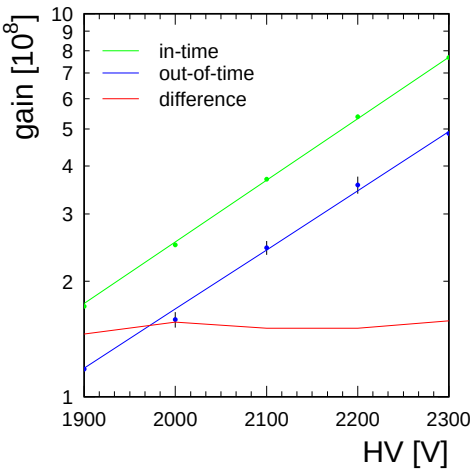

Figure 6.16: *Measured in- and out-of-time gains as a function of the high voltage. The VCSEL was positioned at ($\theta = 0^o$, $\phi = 150^o$).*

fitted with an exponential $G = a \times exp(b \times \mathrm{HV})$, with $a = 1.53 \times 10^5 \pm 2.26 \times 10^5$, $b = 0.0037 \pm 0.0067$ for the in-time, and $a = 1.37 \times 10^5 \pm 3.16 \times 10^5$, $b = 0.004 \pm 0.001$ for the out-of-time.

The in-time gain is about a factor 1.5 ± 0.4 larger than the out-of-time gain.

The value of the in-time gain at 2000 V is 2.5×10^8. Comparing this with the calculated value of 6.7×10^9 (see table 3.2 in chapter 3), we find that the measured gain is about a factor 27 smaller than the calculated gain. This can be caused by a collection efficiency of the interdynode space of less than one (see equation 3.3 in chapter 3).

6.4.3 Gain

The measured gain as a function of the position is shown in figure 6.17. The left plot

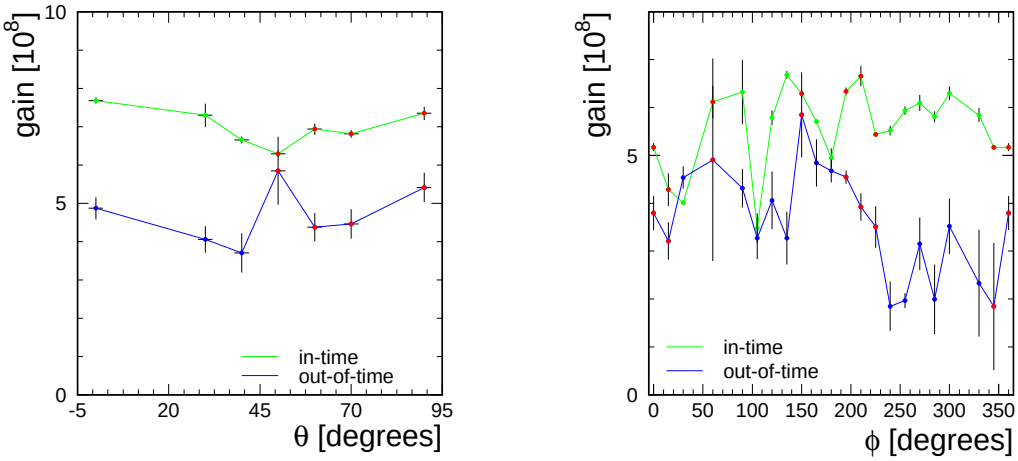

Figure 6.17: *Measured dependence of the in-time and out-of-time gains on θ (left plot), and ϕ (right plot). The gains were obtained at a high voltage of 2300 V.*

shows the variation of the gain with θ. The in-time gain is larger than the out-of-time for each θ value. It is on average a factor 1.5 ± 0.4 larger. The difference is minimum at 50^o: 1.1 ± 0.2.

With red dots the gain values belonging to the θ angles at which the average number of out-of-time pe's is larger than the average number of in-time pe's, are marked. The figure shows that for the in-time and out-of-time gain this is not the case. At $\theta = 50^o$, the position at which the average number of in-time and out-of-time pe's is about the same, both gains have also about the same value.

The gain as funcion of ϕ for both the in-time and out-of-time spectra is shown in the right plot of figure 6.17. From the figure we see that the in-time gain is always larger than the out-of-time , except for $\phi = 30^o$. At this position, and at the positions $\phi = 105^o$ and $\phi = 180^o$ there are dips in the in-time gain. As can been seen from figure 6.14 $\phi = 30^o$ and $\phi = 180^o$ are each others mirror image, and $\phi = 105^o$ lies on the axis of symmetry. Apparently these are not just positions, and the drop of gain is connected to mechanical details of the PMT.

On average the in-time and out-of-time gains differ a factor 1.7 ± 0.2. The difference is minimum at $\phi = 30^o$ (0.88 ± 0.04) and maximum at $\phi = 255^o$ (3.0 ± 0.2).

The gain values belonging to the ϕ values at which the average number of out-of-time pe's is larger than the average number of in-time pe's are marked with red dots. For the gains this could be the case at $\phi = 60^o$, and $\phi = 150^o$, due to large errors in the fit. For the other points marked red this is not the case. At $\phi = 105^o$, the in-time and out-of-time gain is about the same.

6.4.4 Peak to valley ratio

Figure 6.18 shows the P/V ratios. The left plot shows the variation with θ. The average value for the in-time spectra is 5.8 $\pm$ 0.4. The SPE events are well distinguishable from noise, and not well multiplied events. The average value for the out-of-time spectra is 1.1 $\pm$ 0.4. These events are difficult to distinguish from background events.

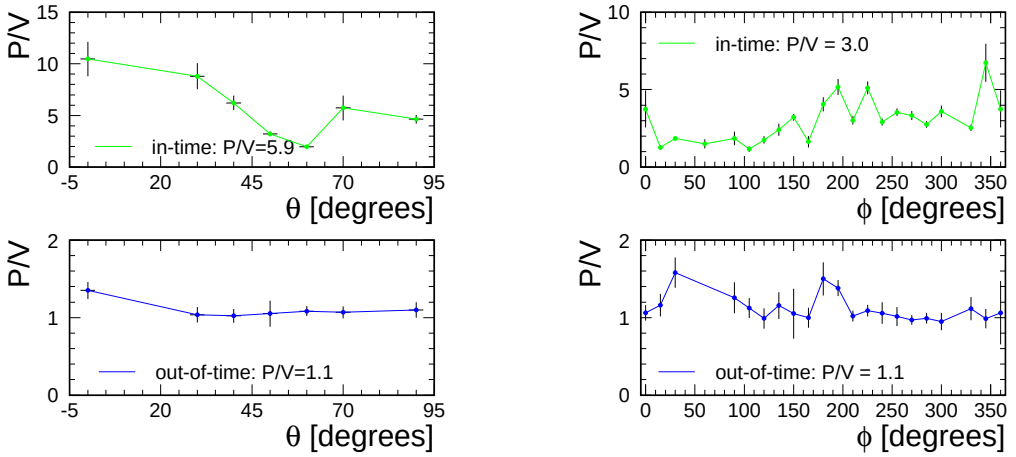

Figure 6.18: *Measured dependence of the in- and out-of-time P/V ratio on θ (left plot), and ϕ (right plot). The high voltage was 2300 V.*

The right plot shows the variation with ϕ. The average value for the in-time spectra is 3.0 $\pm$ 0.2. The SPE events are well distinguishable. This, however, is not the case for the out-of-time events, which have an average P/V ratio of 1.1 $\pm$ 0.2.

From the above we can conclude that the P/V ratio of the in-time distribution is good: the events are well distinguishable from noise, and not well multiplied events. This is not the case for the out-of-time distributions. With its average value of 1.1 the P/V ratio is bad.

6.4.5 Energy Resolution

The enery resolution values were found by dividing the FWHM of the fitted spectra by their peak position. Figure 6.19 shows the variation with θ (left plot), and ϕ (right plot). As could be expected from the P/V results, the resolution of the out-of-time spectra is bad: an average value of 1.2 $\pm$ 0.4 for the θ dependence, and an average

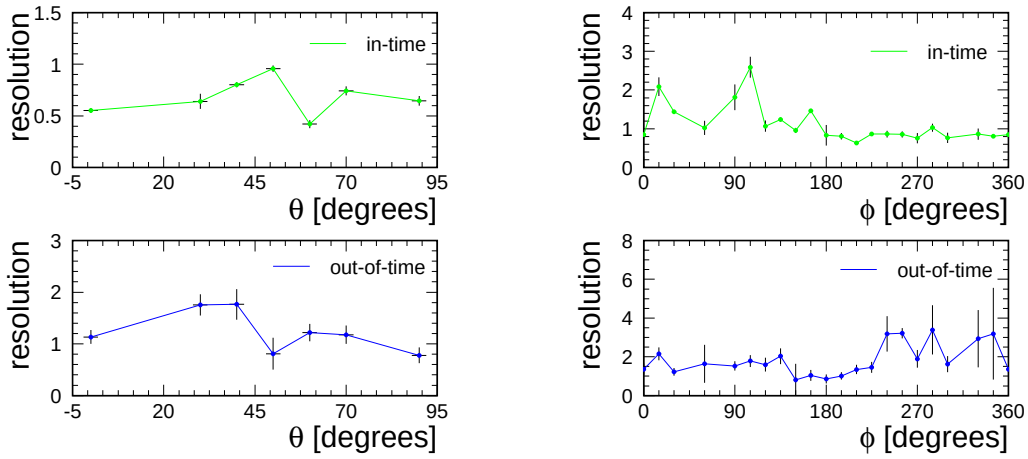

Figure 6.19: *Measured dependence of the in- and out-of-time energy resolution on θ (left plot), and ϕ (right plot). The high voltage was 2300 V*

value of 1.8 ± 0.2 for the ϕ dependence. The in-time resolution is better: an average value of 0.7 ± 0.4 (θ), and 1.1 ± 0.2 (ϕ).

The energy resolution for the in-time distributions, with an average value of 0.9 ± 0.4, is high but with its error of 0.4 not in disagreement with the calculated value of 0.6 (see paragraph 3.4.1 in chapter 3). The resolution is worse for the out-of-time disributions.

6.5 B-field

A mu-metal cage was unfortunately not available for protecting the PMT from the influence of external magnetic fields. To see if, and how the external magnetic fields affect the arrival time, the average number of pe's and the gain, measurements have also been done at the positions (θ = -50^o, ϕ = 150^o), and (θ = -50^o, ϕ = 90^o). The position (θ = -50^o, ϕ = 150^o) indicates the same point on the surface of the PMT as (θ = 50 ^{o}, ϕ = 330^o). The orientations of the PMT towards the total external field, however, are different: to get from θ = 50^o to θ = -50^o, the PMT has to be rotated through a ϕ-angle of 180^o. The position (θ = -50^o, ϕ = 90^o) indicates the same point as (θ = 50^o, ϕ = 270^o), again the orientations of the PMT are different. The results are shown in table 6.1, and table 6.2.

From the tables we see that mostly the in-time pulses are affected by the external magnetic fields: the differences in arrival time are 2 ± 0.6 ns (table 6.1), and 0.6 ± 0.6 ns (table 6.2) opposed to differences of 0.9 ± 0.6 ns (table 6.1), and 0.3 ± 0.6 ns (table 6.2) for the out-of-time.

The gains differ a factor 1.24 ± 0.03 (table 6.1), and 1.26 ± 0.02 (table 6.2) for the in-time distribution, and a factor 1.7 ± 0.8 (table 6.1), and 1.2 ± 0.1 (table 6.1) for the out-of-time.

	$\theta = 50^o \pm 2^o$, $\phi = 330^o \pm 2^o$	θ = -$50^o \pm 2^o$, $\phi = 150^o \pm 2^o$
t_{in}(ns)	7.7 ± 0.4	5.7 ± 0.4
t_{out}(ns)	9.7 ± 0.4	8.8 ± 0.4
pe_{in}	0.011 ± 0.002	0.010 ± 0.001
pe_{out}	0.003 ± 0.001	0.004 ± 0.001
$gain_{in}$	$5.8\times10^8 \pm 0.1\times10^8$	$7.2\times10^8 \pm 0.1\times10^8$
$gain_{out}$	$2.3\times10^8 \pm 1.1\times10^8$	$4.0\times10^8 \pm 0.3\times10^8$

Table 6.1: *Measured values of the in-time and out-of-time arrival times, average number of photoelectrons (pe's) and gains at the same point on the surface of the PMT, but at two different orientations of the PMT towards the total external magnetic field. Values obtained at a HV of 2300 V.*

	$\theta = 50^o \pm 2^o$, $\phi = 270^o \pm 2^o$	θ = -$50^o \pm 2^o$, $\phi = 90^o \pm 2^o$
t_{in}(ns)	6.1 ± 0.4	5.5 ± 0.4
t_{out}(ns)	9.0 ± 0.4	8.7 ± 0.4
pe_{in}	0.010 ± 0.002	0.008 ± 0.001
pe_{out}	0.0020 ± 0.0007	0.0035 ± 0.0008
$gain_{in}$	$6.1\times10^8 \pm 0.2\times10^8$	$7.7\times10^8 \pm 0.1\times10^8$
$gain_{out}$	$3.2\times10^8 \pm 0.5\times10^8$	$3.8\times10^8 \pm 0.3\times10^8$

Table 6.2: *Measured values of the in- and out-of-time arrival times, average number of photoelectrons (pe's), and gains at the same point on the surface of the PMT, but at two different orientations of the PMT towards the total external magnetic field. Values obtained at a HV of 2300 V.*

The difference in the average number of pe's is 0.001 ± 0.002 (table 6.1), and 0.002 ± 0.002 (table 6.12) for the in-time, and 0.001 ± 0.001 (table 6.1), and 0.0015 ± 0.001 (table 6.2) for the out-of-time. The average number of in-time and out-of-time pe's is not affected by the external magnetic fields.

6.6 Late pulses

A distribution of pulses is seen 53.8 ns after the distribution of the main pulses (figure 6.20). According to table 3.3 in chapter 3 these are late pulses. They are produced when the photoelectron is intercepted and reflected by the potential grids before it reaches the first dynode.

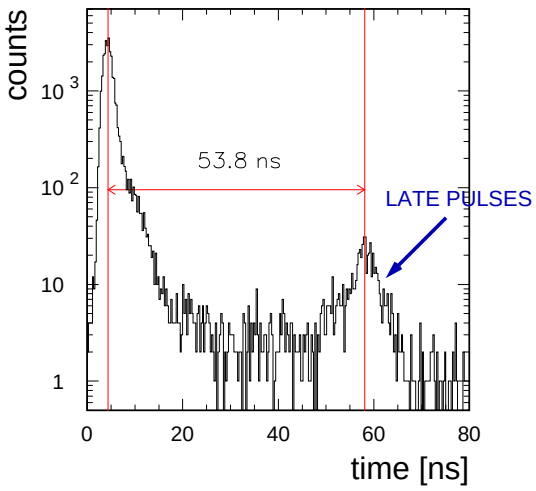

Figure 6.20: *Time distribution of late pulses, 53.8 ns after the main distribution, obtained at (θ = 50º, ϕ = 150º) and a HV of 2300 V.*

6.7 Summary

Table 6.3 gives a summary of some of the results. From the table we see that the arrival

	in-time	out-of-time	Δ_{in-out}
θ			
t(ns)	5.5 ± 0.4	9.0 ± 0.4	3.5 ± 0.4
Δt(ns)	2.0 ± 0.4	2.0 ± 0.4	
G	7.0 ± 0.4×10^8	4.7 ± 0.4×10^8	1.5 ± 0.4
ϕ			
t(ns)	6.2 ± 0.2	9.4 ± 0.2	2.9 ± 0.2
Δt(ns)	constant	constant	
G	5.6 ± 0.2×10^8	3.6 ± 0.2×10^8	1.7 ± 0.2

Table 6.3: *The average values of the arrival time and gain of the in-time and out-of-time distributions for the θ and ϕ scan. The last column shows the difference between the in-time and out-of-time values, for the gain the factor between in-time and out-of-time is shown. The value of the variation of the arrival time with θ and ϕ is also shown. The HV was 2300 V.*

time of both the in-time as out-of-time pulses shows a variation of 2.0 ± 0.4 ns with θ, but no variation with ϕ.

The difference in arrival time between the in-time and out-of-time pulses is about

3 ns. A possible cause for the lateness of the out-of-time pulses are reflections of the photons between first dynode and photocathode. With a distance of about 14 cm between first dynode and photocathode, and a light velocity of 3×10^8 ms^{-1} there should be about seven reflections to get a time difference of 3 ns. At each reflection there will be a probability for the emittance of a photoelectron. Thus in the time-distribution the contribution of each reflection should be visible. This is, however, not the case, and reflections can not be the cause of the out-of-time pulses.

The out-of-time gain is about a factor 1.5 lower than the in-time gain. This, and the fact that the out-of-time charge and time distributions hardly seem to be influenced by the external magnetic fields might lead to the conclusion that the out-of time pulses originate in processes which take place in the dynode system. Since for probing the PMT a light source was used with the wrong wavelength and only thanks to the huge bombardment of photons on the PMT conversion into a photoelectron took place, a lot of unconverted photons enter the PMT. These photons will be for example converted by the first dynode. They do not feel the influence of the external magnetic fields, which is most felt in the electron-optical input system. This can explain the drop in gain and the fact that the external magnetic fields have no affect. The problem with this hypothesis lies in the fact that the out-of-time distribution comes later than the in-time distribution. Photons, which travel with the speed of light, will always arrive earlier on the photocathode than the photoelectrons. Thus pulses caused by photons, converted by the first dynode, should be earlier and not later than the in-time pulses, and we have to disregard this explanation as being the right one.

Furthermore we can state that we are not dealing with afterpulses since these arrive 25-16000 ns after the main pulses (see paragraph 3.4.5 in chapter 3), and since the time distribution changes with the position of the VCSEL on the surface of the PMT, we can also dismiss both VCSEL and electronics as a possible cause. The supply voltage, with its value of 2300 V, exceeds the 2000 V mark, which is given by Hamamatsu as the maximum operating value [23]. However, at lower voltages, we have done measurements from 1900 V to 2300 V, the out-of-time pulses are still present, and thus the HV can be disregarded as a possible cause.

Above we have dismissed the VCSEL, including its wavelength, as a possible candidate for the occurrence of the out-of-time pulses. A possible reason why we did not see these pulses when we used the blue LED as light source (see figure 6.4) is the large width of the source. The out-of-time pulses can be there but the double peak stucture of the time spectrum is just not visible.

Although we have not found an exact cause for the out-of-time pulses, there are definitely good indications that it lies within the PMT: the angular regions $345^o \leqq \phi \leqq 15^o$, $195^o \leqq \phi \leqq 225^o$, and the angles ϕ=60^o, and ϕ=150^o, for which the average number of out-of-time pe's is larger than the average number of in-time pe's correspond to mechanical details of the PMT (see figure 6.14). Furthermore the TTS of the out-of-time distribution is low (3.9 $\pm$ 0.2 ns) compared to the other regions (6.6 $\pm$ 0.2 ns). This again can indicate that we are dealing with processes that take place in the dynode system, since the width of the TTS is mostly formed in the electron-optical input system (see paragraph 3.4.2 in chapter 3). If this is the case the TT of the out-of-time pulses in these regions should be smaller than in the other regions, and the gain should

be lower. This is not the case as can be seen in figures 6.11 and 6.17, although it must be noted that it was difficult to fit the out-of-time charge spectrum.

The average number of in-time pe's decreases from center to edge. The average number of out-of-time pe's keeps quite constant with θ. For $\theta > 50^o$ the average number of out-of-time pe's is equal or larger than the average number of in-time pe's. The in-time and out-of-time gains are also about the same at $\theta = 50^o$. Apart from this angle, there does not seem to be a relation between the gain and the average number of pe's, and the gain can not be the cause of the variation in the average number of pe's. It must again be noted that it was much more difficult to fit the out-of-time charge spectra than the time spectra (see paragraph 6.4.4 for the P/V ratios, and paragraph 6.4.5 for the energy resolution values).

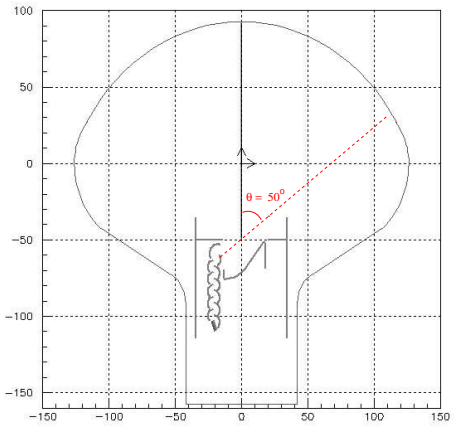

Figure 6.21: *View of the position of the point on the surface of the PMT for which* θ *=* 50^o *[24].*

The region $\theta > 50^o$ is not just a region as can be seen from figure 6.21: it lies within the line of sight of the second dynode, with for $\theta > 63^o$ a small panel obstructing the line of sight. The percentage out-of-time pe's for the position $\theta = 50^o$ is 43 % (see figure 6.13), for the position θ = -50^o it is 29 % (see table 6.1). Thus for θ = -50^o, which lies within the line of sight of the first dynode, the percentage out-of-time pe's is lower than for $\theta = 50^o$.

We can conclude that, although we do not know what the exact cause of the out-of-time pulses is, that it has something to do with the mechanical details of the PMT.

Chapter 7

Conclusion and Outlook

A study has been made to see if and how the characteristics of the ANTARES PMT change as a function of the impact point of the light beam. For every impact point a double peaked structure for the time distribution was found. Each distribution could be fitted well with two Gaussians. The pulses in the second Gaussian distribution, the so-called out-of-time pulses, arrive on average 3 ns later than the pulses in the first Gaussian distribution, the so-called in-time pulses. For both in-time and out-of-time pulses a variation with θ of 2 ns, and no variation with ϕ was found (see chapter 5 for the definition of the angles).

The charge distribution could also be split into an in-time and out-of-time part. Both in-time and out-of-time distributions were fitted with a Gaussian. The in-time gain was on average a factor 1.5 higher than the out-of-time gain. No explicit variation with the position of the impact point was found.

The average number of out-of-time photoelectrons was found to be larger than the average number of in-time photoelectrons for the regions $\theta > 50^o$ (ϕ=150^0), $345^o \leqq \phi \leqq 15^o$ (θ=50^0), $195^o \leqq \phi \leqq 225^o$ (θ=50^0), and the angles (ϕ=60^o, θ=50^0) and (ϕ=150^o, θ=50^0). The transit time spread in these ϕ- regions is low (3.9 ns) compared to the other ϕ-regions (6.6 ns).

The in-time pulses are the output pulses that we expect a PMT to have. The out-of-time pulses should not be there. In the summary of chapter 6 we have introduced some possible causes of these pulses including reflections between photocathode and first dynode. All of these have been disregarded and a correct explanation has not been found. It must, however, be noted that the measurements were done without a mu-metal cage and with a light source with a wavelength of 850 nm. At this wavelength the quantum efficiency of the PMT is very low (see figure 3.3 in chapter 3). It will be best to repeat the measurements with a mu-metal and a light source with a wavelength of about 450 nm. This is the wavelength around which the spectrum of Čerenkov light is centered (see section 4.2), and with which the PMT has to deal in the ANTARES detector. Furthermore, the light source should have a width much smaller than the FWHM of the time distribution of the PMT. The University of Sheffield, also in the ANTARES collaboration, has a nanoled, which generates picoseconds pulses, and has a wavelength which lies in the blue region of the spectrum (430 to 445nm).

Unfortunately, at the time of our measurements, it was used elsewhere and could not be employed. If future tests will be done, we recommend to use this source.

If with a mu-metal cage and the right light source there are still out-of-time pulses, we have to conclude that there is a problem for the above mentioned regions and angles: the ANTARES project uses a precision of $\sim$ 1 ns in its track reconstruction programs (see paragraph 2.5 in chapter 2), and can not afford inaccuracies of 3 ns. Furthermore the 2 ns variation with θ of the transit time for both the in-time and out-of time pulses is too high for a 1 ns precision.

To get a more accurate map of the problem regions, a more thorough scan of the surface of the PMT should be made. For this it is recommended to have an automatic setup that does not have to deal with reopening the black box every time the light source has to be repositioned. Waiting for the PMT to calm down after closing the black box is a time consuming process (timeconstant 8.5 hrs, see section 6.2.1).

Finally we like to finish with figure 6.14 in paragraph 6.3.5, which shows the front of the PMT including the problem areas. From the figure we see that these areas are not just accidental but correspond to the mechanical details of the PMT. This tends us to conclude that the cause of the out-of-time pulses lies within the PMT.

Bibliography

[1] John Lankford, History of Astronomy, an encyclopedia, Garland Publishing, Inc (1997).

[2] Sir James Jeans, The universe around us, Cambridge University Press (1930).

[3] Joseph Ashbrook, The Astronomical Scrapbook, Cambridge University Press (1984).

[4] European Southern Observatory, The VLT White Book, European Southern Observatory (1998).

[5] B.P. Venemans et al., The most distant structure of galaxies known: a protocluster at z = 4.1, Astrophys. Journal Lett 569 (2002), L11.

[6] K. Greisen, Phys. Rev. Lett. 16 (1966) 748; G.T. Zatsepin and V.A. Kuz'min, JETP Lett. 4 (1966) 78; R.J. Gould and G.P. Schreder, Phys. Rev. Lett. 16 (1966) 252.

[7] David Griffiths, Introduction to elementary particles, John Wiley & Sons, inc. (1987).

[8] M.A. Markov, Proc. 10 International Conference on High Energy Physics in Rochester, (1960) 579;

[9] The Baikal Collaboration, The Baikal Deep Underwater Neutrino Experiment Status Report, Phys.Atom.Nucl. 61 (1998) 886-896.

[10] R. Wischnewski for the AMANDA Collaboration, The AMANDA-II Neutrino-Telescope, astro-ph/0204268.

[11] A. Capone, on behalf of the ANTARES collaboration, The ANTARES Neutrino Telescope: Status report, ICRC 2001.

[12] The ANTARES Collaboration, A Deep Sea Telescope for High Energy Neutrinos, astro-ph/9907432.

[13] The ANTARES Collaboration, Technical design report of the ANTARES 0.1 km^2 project, version 1.0, 2001.

[14] E. Carmona, J.J. Hernández, A new reconstruction technique for ANTARES, ANTARES-Soft/ 2000-11.

[15] N. Palanque-Delabrouille, Optical background measurements, Test 1.10 in the ANTARES site, ANTARES-Site/2000-003.

[16] Sir Edmund Whittaker, A history of the theories of aether and electricity, volume 1: the classical theories, Harper Torchbooks/ The Science Library (1960), p 356.

[17] A. Einstein: Ann. Physik, 17, (1905) 132.

[18] H. Bruining, Physics and applications of secondary electron emission, Pergamon press ltd (1954), p. 1.

[19] Hamamatsu Photonics K.K, Photomultiplier tube, Hamamatsu Photonics K.K. (1994).

[20] Hamamatsu specification sheets for tube R5912, via http://www.hamamatsu.com.

[21] C. Arpesella, Test results of 14 stages 8″ Hamamatsu photomultiplier, ANTARES-OM-97-5, internal note, p 21.

[22] Philips Photonics, photomultiplier tubes, Philips photonics (1994).

[23] Hamamatsu tentative data, Photomultiplier tube R7081-20, via Technical design report of the ANTARES 0.1 km^2 project, 2001.

[24] Herve Lafoux, private communication.

[25] M. Karolak, Test results of 80 10″ Hamamatsu PMT, ANTARES-Opmo/2000-007, internal note, 3.

[26] Hamamatsu photomultiplier tube test sheet, serial number: ST5164.

[27] V.P. Zrelov, Cherenkov radiation in high-energy physics, part 1, Israel Program for Scientific Translations (1970).

[28] R.C. Fernow, Introduction to experimental particle physics, Cambridge University Press (1989) 181.

[29] P. Amram et al., The ANTARES Optical Module, astro-ph/0112172 (Dec 2001).

[30] D.J.L. Bailey, The effect of the group velocity and dispersion on photon arrival times in the ANTARES detector, internal report ANTARES-Phys/2001-01.

[31] J.E. MacMillan, Using the Sheffield Pulser, private communication.

[32] Kapustinsky et al., A fast timing light pulser for scintillation detectors, Nucl.Instr. and Meth., A241:612-613 (1985).

Dankwoord

Mijn afstudeerstage zou zeker niet zo leuk en leerzaam zijn geweest zonder de hulp van Jos Steijger en Erwin Kok.

Jos kan ik niet genoeg bedanken voor het op zich nemen van de begeleiding, voor de deur die altijd openstond en het nooit ongelegen zijn van mijn vragen. Van hem heb ik ontzettend veel geleerd zowel tijdens de stage als bij het schrijven van de scriptie.

Erwin wil ik bedanken voor zijn hulp tijdens de beginfase, zijn bereidheid tot uitleg en zijn betrokkenheid bij het werk.